

The vanadium Magnéli phases V_nO_{2n-1}

Udo Schwingenschlögl* and Volker Eyert

Institut für Physik, Universität Augsburg, 86135 Augsburg, Germany

Received 18 March 2004, accepted 26 March 2004 by U. Eckern

Key words Magnéli series, transition metal oxides, vanadium dioxide, vanadium sesquioxide

PACS 71.10.Fd, 71.10.Pm, 71.45.-d

To compare the metal-insulator transitions (MITs) of VO_2 and V_2O_3 we analyze the relations between the structural and electronic properties of the vanadium Magnéli phases. These materials set up the homologous series V_nO_{2n-1} ($3 \leq n \leq 9$) and have crystal structures comprising typical dioxide-like and sesquioxide-like regions. As the MITs of the vanadium Magnéli phases are accompanied by structural transformations, we are able to discuss the effects of characteristic changes in the local atomic environments. The systematic investigation of the transport properties is based on a new and unifying description of the crystal structures of the Magnéli phases including VO_2 and V_2O_3 . Our results lead to a comprehensive understanding of the MITs in the Magnéli class and shed new light on the role of particular electronic states for the MIT of V_2O_3 .

Contents

1	Introduction	1
2	Crystal structure and electronic properties of VO_2 and V_2O_3	4
3	Crystal structures of the Magnéli phases: a unified representation	9
4	Structural and calculational details	13
5	Dimerization and localization in V_6O_{11}	18
6	Band narrowing in V_4O_7	25
7	Systematic aspects of the Magnéli series	30
8	Conclusions	34
	References	35

1 Introduction

The vanadium oxides [1–3] comprise compounds with different formal vanadium valency stages, which reach from two in VO , three in V_2O_3 , and four in VO_2 to five in V_2O_5 . In addition to these configurations mixed valent compounds can be synthesized. Amongst the latter the so-called Magnéli phases, defined by the general stoichiometric formula

$$V_nO_{2n-1} = V_2O_3 + (n-2)VO_2 \quad \text{where } 3 \leq n \leq 9, \quad (1)$$

* Corresponding author E-mail: Udo.Schwingenschloegl@Physik.Uni-Augsburg.de, Fax: +49 821 598 3262
Online colour figures at: www.ann-phys.org

Compound V_nO_{2n-1}	Parameter n	Formal V $3d$ charge	MIT temperature
V_2O_3	2	2	168 K
V_3O_5	3	$5/3 \approx 1.67$	430 K
V_4O_7	4	$6/4 \approx 1.50$	250 K
V_5O_9	5	$7/5 \approx 1.40$	135 K
V_6O_{11}	6	$8/6 \approx 1.33$	170 K
V_7O_{13}	7	$9/7 \approx 1.29$	metallic
V_8O_{15}	8	$10/8 \approx 1.25$	70 K
V_9O_{17}	9	$11/9 \approx 1.22$	—
VO_2	∞	1	340 K

Table 1 Formal V $3d$ charges as well as transition temperatures in the series V_nO_{2n-1} .

are of special interest since they give rise to a homologous series of compounds with closely related crystal structures. This type of homologous series has been reported for the first time by Magnéli for the molybdenum oxides [4]. Nowadays additional Magnéli series are known for the vanadium, titanium, niobium, and tungsten oxides. The first structural characterization of vanadium Magnéli compounds by means of x-ray investigations traces back to Andersson and Jahnberg [5] in 1963. As equation (1) indicates, the Magnéli phases take an intermediary position between V_2O_3 and VO_2 , thus between the valency stages three and four. In addition to the chemical relationship, the crystal structures of the Magnéli phases actually consist of rutile and corundum-type blocks and consequently show structural affinity to both the dioxide and the sesquioxide. In section 3 we study the structural relations between these materials in detail – discovering the potential of gradually transferring the crystal structure of VO_2 into that of V_2O_3 by making use of the Magnéli phases. This observation allows for a comprehensive understanding of all these compounds.

As a function of temperature each Magnéli phase undergoes a metal-insulator transition (MIT), except for V_7O_{13} , which is metallic at all temperatures. The MITs are of first order and accompanied by distinct structural transformations. Table 1 summarizes transition temperatures, inferred from electrical resistivity measurements by Kachi et al. [6], and formal V $3d$ charges, varying from two in V_2O_3 to one in VO_2 . In an ionic picture a metal atom contributes three $3d$ and two $4s$ electrons, whereas an oxygen atom accepts two $2p$ electrons. As the Magnéli phases are characterized by vanadium atoms in mixed valent states, the electronic properties were expected to be influenced by charge ordering. Although this is interesting from both the experimental and theoretical point of view, only few studies are reported in the literature.

Figure 1 illustrates the behaviour of the MIT temperatures listed in table 1 as a function of the vanadium-oxygen ratio. We recognize a broad minimum centered at the ratio corresponding to V_7O_{13} . Interestingly, the MITs of the vanadium Magnéli phases are coupled to an anomaly in the magnetic susceptibility, which closely resembles the characteristics of a transition from a paramagnetic to an antiferromagnetic state [6]. Nonetheless, the anomaly is not accompanied by long range magnetic order. Yet, all Magnéli phases enter an antiferromagnetic groundstate at sufficiently low temperatures; Néel temperatures are given in figure 1. In some sense the anomaly may be interpreted as a precursor effect. There is a maximum of the transition temperature for V_2O_3 and a gradual decrease on approaching VO_2 , where antiferromagnetic ordering is no longer observed. V_7O_{13} is the only deviation from this general trend. Although a continuous reduction of V_2O_3 -like regions in the crystal structure is a possible explanation for decreasing transition temperatures, this kind of mechanism has not been confirmed. While MIT and magnetic ordering are coupled for V_2O_3 , they appear at different temperatures and thus are likely to occur independently for other Magnéli phases. As we are interested in the MITs, the subsequent electronic structure calculations do not take into account the low temperature antiferromagnetism. Actually, it would not be possible to include the magnetic order since the detailed magnetic structures of the ordered phases are not known.

Specific heat data for the Magnéli phases by Khattak et al. [7] revealed values larger than expected from pure lattice contributions. Due to the smallness of the magnetic entropy increase at the Néel temperatures

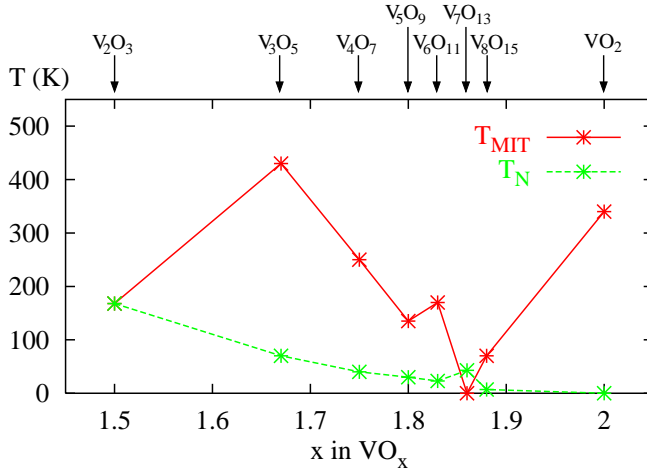


Fig. 1 Comparison of the MIT temperatures and the magnetic ordering temperatures of the Magnéli phases. Besides V_7O_{13} all members of the series undergo an MIT. Except for VO_2 each compound develops an antiferromagnetic order at low temperatures. In the case of V_2O_3 the MIT and the magnetic ordering coincide at a temperature of 168 K.

the authors argued in favour of magnetic correlations above the phase transitions. To explain their findings they proposed a model based on linear antiferromagnetic chains. However, low temperature investigations of the magnetic susceptibility by Nagata et al. [8] ruled out this model. The authors suggested interpreting insulating V_8O_{15} in terms of a charge-density wave, as Gossard et al. [9] speculated in the case of V_4O_7 . They attributed small magnetic moments at the metal sites of insulating V_4O_7/V_6O_{11} to singlet pairing.

Single crystal x-ray data by Marezio et al. [10] indicated chains of V^{3+} and V^{4+} ions in the insulating phase of V_4O_7 , whereas the vanadium valences are disordered in the metallic phase. This kind of evidence for charge localization arises from the comparison of experimental V-O distances in V_4O_7 with estimated values referring to an ionic picture. VO_6 units with large/small V-O bond lengths are interpreted in terms of V^{3+}/V^{4+} configurations, respectively. However, due to the covalent portion of the interatomic bonding the calculated charges might be poor. Specific heat data by Griffing et al. [11, 12] implied that metallic V_4O_7 and V_7O_{13} are characterized by a coexistence of itinerant and localized V 3d electrons. Nuclear magnetic resonance experiments confirmed this result and additionally found two inequivalent metal sites, but were in conflict with pure $S = 1/2$ and $S = 1$ spin states, corresponding to d^1 and d^2 configurations [9, 13]. In the insulating phase the Magnéli compounds show indications of increased charge localization and singlet pairing, except for V_3O_5 . The charge localization may split the subbands associated with the inequivalent metal sites and hence may pave the way for a Mott–Hubbard transition.

While the MIT temperature of VO_2 increases on the application of pressure, V_2O_3 reveals the opposite trend. The Magnéli phases reflect the behavior of the sesquioxide as their transition temperatures decrease with growing hydrostatic pressure [2]. Moreover, Canfield et al. [14] reported on unifying aspects emerging in the Magnéli series on the application of pressure. They observed for both V_8O_{15} and $(V_{0.98}Cr_{0.02})_8O_{15}$ a transition from a paramagnetic metal (PM phase) to an antiferromagnetic metal (AFM phase) and further to a paramagnetic insulator (PI phase). Consequently, the PM-AFM transition present for V_7O_{13} at atmospheric pressure should not be regarded anomalous for the Magnéli series. While the PM-AFM transition is found in V_8O_{15} only above 9 kbar, it is always present for the chromium doped system. The magnetic transition exhibits the same pressure dependence in all three cases (-0.75 K/kbar). Since the MIT temperature decreases at a larger rate, the AFM modification is stabilized for sufficiently high pressures. Although in other Magnéli phases the PM-AFM transition is not observed up to 20 kbar, the authors assume different pressure dependences of the MIT and the antiferromagnetic ordering as a general feature, common to each Magnéli phase. This again indicates that the transitions evolve independently.

2 Crystal structure and electronic properties of VO_2 and V_2O_3

Above 340 K VO_2 crystallizes in the rutile crystal structure based on a simple tetragonal lattice with space group $P4_2/mnm$ (D_{4h}^{14}), as shown in figure 2. Using single crystal experiments McWhan et al. [15] determined the tetragonal lattice constants $a_R = 4.5546 \text{ \AA}$ and $c_R = 2.8514 \text{ \AA}$ and the positional parameters. With respect to the vanadium sites the VO_2 structure is based on a body-centered tetragonal lattice, where each metal site is surrounded by an oxygen octahedron. Octahedra at the center and the corners of a rutile unit cell are rotated by 90° around the rutile c -axis. This reduces the lattice symmetry from body-centered tetragonal to simple tetragonal and causes the unit cell to contain two formula units. Equally adjusted octahedra form chains along the rutile c -axis. Within the chains neighbouring octahedra share edges, whereas corner and center chains are connected via corners. Next to the filled oxygen octahedra the VO_2 structure comprises the same amount of empty octahedra, which likewise form chains along the rutile c -axis. Hence VO_2 is based on a regular three dimensional network of oxygen octahedra partially filled with vanadium atoms. Each octahedron has orthorhombic symmetry, but deviations from tetragonal and even cubic symmetry are small. One observes two different V-O distances, where the apical distance appears twice within each octahedron and the equatorial distance is found four times [16].

We define local coordinate systems centered at the metal sites. Because of the different orientations of the oxygen octahedra two reference systems are required. In both cases the local z -axis is oriented along the apical axis of the (local) octahedron, which is either the (110) or the $(1\bar{1}0)$ direction. Compared to the traditional alignment of the local x and y -axis parallel to the metal-ligand bonds, these axes are rotated by 45° around the local z -axis. Thus they are parallel and perpendicular to the rutile c -axis, respectively. This definition of a local rotated reference frame is useful not only for rutile VO_2 but also for related structures. Referring to the original rutile coordinates we introduce the pseudorutile axes a_{prut} , b_{prut} and c_{prut} , which allows us to discuss the crystal structures of the different Magnéli phases on a common basis.

Figure 3 displays the angular parts of the metal d orbitals relative to the reference frame of the central metal atom. The cubic part of the crystal field splitting results in a separation of the d orbitals in threefold degenerate t_{2g} ($d_{x^2-y^2}$, d_{xz} , d_{yz}) and twofold degenerate e_g ($d_{3z^2-r^2}$, d_{xy}) states. While both e_g orbitals point to oxygen atoms, the $d_{x^2-y^2}$ orbital points along the rutile c -axis (local x -axis) and the local y -axis. Moreover, d_{xz}/d_{yz} orbitals are directed to faces of the local oxygen octahedron. Hence σ and π -type V-V overlap along the rutile c -axis is mediated by $d_{x^2-y^2}$ and d_{xz} states, respectively. Due to the 45° rotation of our coordinate system the $d_{x^2-y^2}$ and d_{xy} orbitals are interchanged compared to the standard notation. The lobes of the d_{yz} orbital point perpendicular to the rutile c -axis. Because of the ratio $c_R/a_R = 0.6260$ of the crystal axes they exhibit reduced σ -type overlap, compared to the $d_{x^2-y^2}$ states. While both $d_{x^2-y^2}$ and d_{yz} orbitals connect metal atoms separated by tetragonal lattice vectors, coupling between metal sites at the center and the corners of the unit cell is mediated by d_{xz} orbitals, which exhibit remarkable overlap with the $d_{x^2-y^2}$ states belonging to the vanadium atoms of neighbouring octahedral chains.

The first order phase transition of stoichiometric VO_2 at 340 K is accompanied by structural distortions leading to the monoclinic M_1 phase, which is based on a simple monoclinic lattice with space group $P2_1/c$ (C_{2h}^5) [17]. Despite very similar gross features, distinct differences distinguish rutile and monoclinic VO_2 . First, a characteristic metal-metal pairing along the c_{prut} -axis is present in the monoclinic structure, which modifies the V-V distances (2.851 \AA in the rutile case) and gives rise to alternating values of 2.619 \AA and 3.164 \AA . Second, zigzag-type displacements of the metal sites evolve along the diagonal of the rutile basal plane (local z -axis). The shift direction alternates along $a_{\text{prut}}/c_{\text{prut}}$ but not along b_{prut} . Due to the zigzag-type distortions two different apical V-O bond lengths of 1.77 \AA and 2.01 \AA are observed. In addition, the V-V pairing results in two short (1.86 \AA and 1.89 \AA) and two long (2.03 \AA and 2.06 \AA) equatorial distances in each oxygen octahedron. Third, a lattice strain is present in the monoclinic configuration.

Uniaxial stress along the rutile (110) axis or doping with some percent of chromium/aluminium yields two additional insulating phases: the monoclinic M_2 and triclinic T phase [18–20]. In the M_1 phase V-V pairing and zigzag-type lateral displacements of the metal atoms affect each vanadium chain. In contrast, in the M_2 phase half of the chains dimerize and the other half show zigzag-type deviations. The T phase

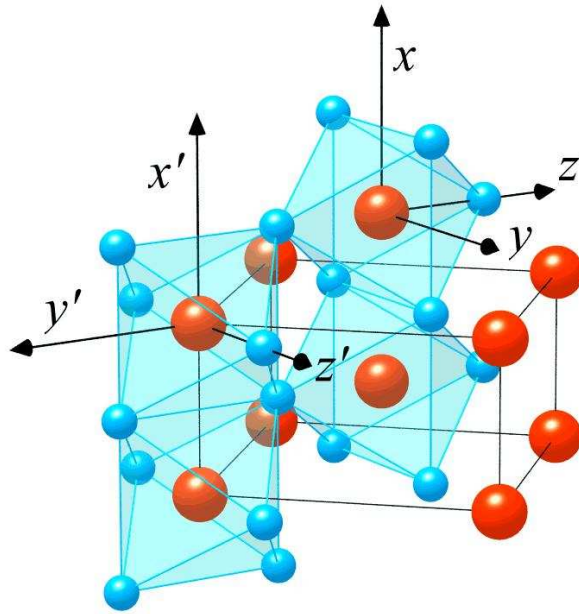


Fig. 2 Crystal structure of metallic VO_2 . The inserted cuboid determines the unit cell of the rutile structure with the c -axis oriented upwards. Large and small spheres represent vanadium and oxygen atoms, respectively. The vanadium atoms form infinite chains along the rutile c -axis. Furthermore, each vanadium site is surrounded by an oxygen octahedron. The latter are oriented uniformly in each vanadium chain but rotated by 90° with respect to the rutile c -axis among neighbouring chains. Hence they establish local coordinate systems.

is intermediate since the dimerized M_2 chains start to tilt and the zigzag chains evolve a dimerization until eventually the M_1 structure is reached.

An instability of the rutile crystal structure is found not only for VO_2 but also applies to other transition metal oxides, as for instance MoO_2 and NbO_2 . For the latter compounds the relations between structural distortions and electronic structure changes have been studied in [22, 23]. As VO_2 , they are characterized by metal-metal pairing and lateral zigzag-type displacements in the low temperature phase. Despite all the similarities a striking difference regarding the in-plane distortions of the metal atoms and the modifications of the surrounding oxygen octahedra distinguishes monoclinic VO_2 and MoO_2 . Only for the latter material the octahedra follow the in-plane metal shifts, whereas for VO_2 the vanadium atoms move relative to their oxygen octahedra. This relative shift affects the bonding between V $3d$ and O $2p$ states as it influences the orbital overlap. Thus an antiferroelectric distortion of the VO_6 octahedra is inherent in the monoclinic (M_1) phase of VO_2 . From the different behaviour of VO_2 and MoO_2 it was concluded that the antiferroelectric distortion cannot explain the tendency of the transition metal oxides to form distorted variants of the ideal rutile structure. For the same reason the mechanism must be excluded as a possible driving force for MITs connected to the destabilization of the rutile crystal structure [24].

Theoretical approaches towards understanding the MIT and the simultaneous structural transformations range from Peierls [25, 26] to Mott–Hubbard [27, 28] schemes. Possible driving forces are lattice instabilities, electron-phonon interaction, and electronic correlations. The importance of the lattice for stabilization of the different phases of VO_2 and the symmetry change at the transition point to strong electron-phonon coupling [15]. This line of reasoning is supported by a comparison of rutile and monoclinic VO_2 via ultrasonic microscopy, which reveals a strong elastic anisotropy in the metallic but almost no anisotropy in the insulating phase [29]. The electronic structure of metallic VO_2 has been probed by optical measurements revealing the lowest empty V $3d$ levels 2.5 eV above the top edge of the O $2p$ bands [30]. Ultraviolet and x-ray photoelectron spectroscopy show a 8.5 eV wide occupied band directly below the Fermi energy [31]. The valence band splits up into low and high binding regions with widths of 1.5 eV and 6 eV, respectively. While the low binding contributions are attributed to the V $3d$ states, the broader part of the valence band mainly traces back to O $2p$ states. According to oxygen K-edge x-ray absorption spectroscopy unoccupied V $3d$ bands extend from the Fermi energy to 1.7 eV and from 2.2 eV to 5.2 eV [32]. For monoclinic VO_2

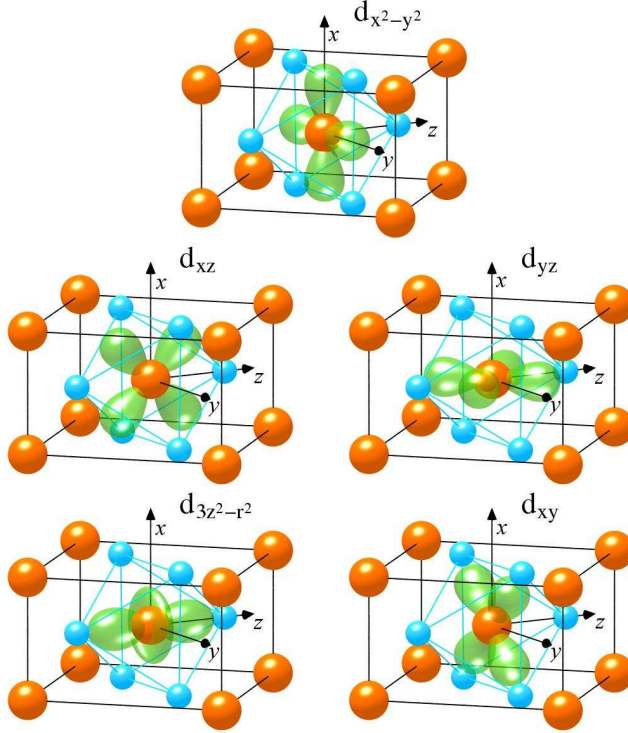


Fig. 3 Angular parts of the transition metal 3d states with respect to the local coordinate system of the central metal atom in the displayed rutile unit cell. Note that the rutile c -axis is oriented upwards. The t_{2g} manifold, resulting from the crystal field splitting of the metal states, comprises the $d_{x^2-y^2}$, d_{xz} and d_{yz} orbitals, whereas the e_g manifold comprises the $d_{3z^2-r^2}$ and d_{xy} states. While the $d_{x^2-y^2}$ lobes point at edges of the local octahedron, the d_{xz} and d_{yz} orbitals are directed towards faces. Both e_g orbitals point at oxygen atoms.

photoelectron spectroscopy shows a sharpening accompanied by an energetical downshift of the occupied V 3d bands. Shin et al. reported a band gap of 0.7 eV for the insulating phase [33].

Goodenough proposed an energy band scheme for both metallic and insulating VO_2 [1]. Starting with electrostatic considerations he placed the O 2p states well below the V 3d states. Octahedral crystal field splitting leads to lower V 3d t_{2g} and higher V 3d e_g levels, where the former are located in the vicinity of the Fermi level and split into $d_{||}$ (oriented parallel to the rutile c -axis) and π^* states. In the monoclinic case metal-metal pairing causes the $d_{||}$ band to split into filled bonding and empty antibonding states. Due to antiferroelectric zigzag-type displacements of the metal atoms, the π^* bands shift to higher energies. Shin et al. found the $d_{||}$ band splitting to amount to 2.5 eV and the π^* bands to rise by 0.5 eV [33]. In contrast to the Goodenough scheme Zylbersztein and Mott proposed an MIT mechanism based on strong electron-electron correlations [34]. According to these authors especially the one-dimensional $d_{||}$ band is affected by correlations rather than by electron-lattice interaction. In the metallic phase correlations are efficiently screened by the π^* electrons, but screening is reduced below the phase transition as the π^* bands are subject to an energetical upshift. Thus the narrow $d_{||}$ bands become susceptible to strong Coulomb repulsion and undergo a Mott-transition – opening a correlation gap. Recently, the MIT of VO_2 was explained in terms of a Peierls instability of the one-dimensional $d_{||}$ band, embedded in a background of the remaining V 3d t_{2g} states [24, 35]. Molecular dynamics calculations by Wentzcovitch et al. likewise point to predominant influence of the lattice degrees of freedom [36].

Stoichiometric V_2O_3 at ambient pressure undergoes an MIT at 168 K accompanied by a transformation from the high temperature corundum into the low temperature monoclinic structure, where additionally an antiferromagnetic order appears (AFI phase). Systematic studies have provided the temperature, pressure, and composition dependence of the MIT in the $(V_{1-x}Cr_x)_2O_3$ system [37, 38]. Doping with chromium or aluminum results in a paramagnetic insulating configuration (PI phase), which retains the lattice symmetry of the paramagnetic metal (PM phase). Since the metal-insulator boundary terminates at a critical point, a gradual PM-PI crossover appears when decreasing the temperature from well above the 500 K region. For

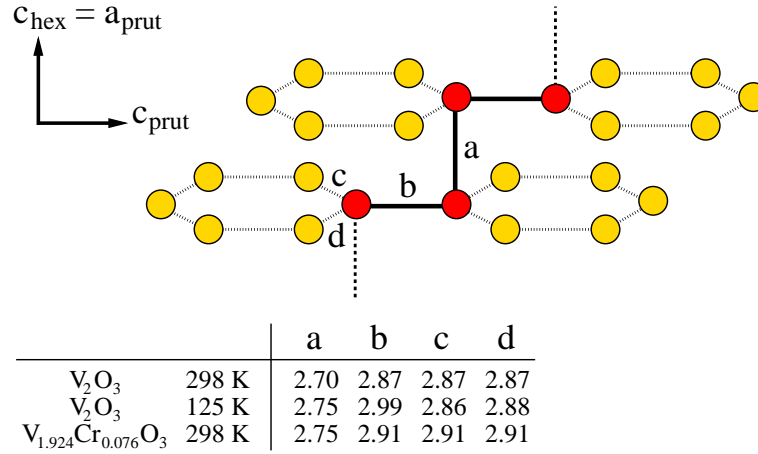


Fig. 4 Crystal structure of V₂O₃. For simplicity the schematic view does not include the oxygen sublattice, which is an octahedral network qualitatively equal to the case of VO₂. The vanadium atoms once more occupy octahedral sites but now form hexagonal structures perpendicular to the c_{hex} -axis. Hence vanadium pairs arise both along $a_{\text{prut}}=c_{\text{hex}}$ and c_{prut} . The table records experimental V-V distances (in Å) for the paramagnetic metallic, the antiferromagnetic insulating, and the paramagnetic insulating phase of V₂O₃ [40,41].

a chromium concentration $0.005 \leq x_{\text{Cr}} \leq 0.018$ three phase transitions are encountered: PM-PI, PI-PM, and PM-AFI, where the last two are of first order [39]. For $x_{\text{Cr}} < 0.005$ the reentrant MIT disappears. In contrast, on doping with titanium the PM-AFI transition temperature decreases and for $x_{\text{Ti}} > 0.05$ only a metallic phase is found. Hydrostatic pressure has almost the same effect as doping with titanium.

Corundum V₂O₃ is based on a trigonal lattice with space group $R\bar{3}c$ (D_{3d}^6). Oftentimes a non-primitive hexagonal unit cell comprising six formula units is used, whereas the primitive trigonal unit cell contains two formula units. The metal atoms are octahedrally coordinated by six oxygen atoms, where the oxygen network is qualitatively equivalent to the arrangement in VO₂. We identify the c_{hex} -axis of the hexagonal unit cell with the a_{prut} -axis. Two thirds of the oxygen octahedra are filled with vanadium, but no continuous chains of face-sharing VO₆ octahedra arise. Instead, two filled octahedra are followed by an empty one. Neighbouring chains are shifted along c_{hex} , giving rise to hexagonal vanadium structures, see figure 4. This forms the basis of describing the corundum structure in terms of a hexagonal cell. Because of the trigonal symmetry each metal atom exhibits three identical in-plane V-V distances of 2.87 Å. Metal-metal electrostatic interaction along c_{hex} (through octahedral faces) causes V-V anti-dimerization reflected by a bond length of 2.70 Å, which is considerably larger than the ideal octahedral separation of 2.33 Å. Hence the hexagonal vanadium structures deviate from being planar. There are three V-O bond lengths of 1.97 Å and three other of 2.05 Å in each VO₆ unit.

At 168 K stoichiometric V₂O₃ distorts into a monoclinic structure with space group $I2/a$ (C_{2h}^6), characterized by increasing nearest neighbour V-V distances [40]. Bond lengths across shared octahedral faces along a_{prut} increase from 2.70 Å to 2.75 Å. Moreover, the threefold degeneracy of the in-plane V-V distance is lifted, giving rise to a strongly elongated (2.99 Å) bond along c_{prut} -axis. The symmetry breaking at the PM-AFI transition results in two crystallographically inequivalent oxygen sites, where each oxygen octahedron comprises four sites of the first and two of the second kind. Although the V-O distance varies from 1.95 Å to 2.11 Å, the average length is similar to the PM phase. In contrast to the symmetry breaking at the PM-AFI transition, the corundum structure is conserved at the PM-PI transition [41]. Nevertheless, V-V bond lengths across octahedral faces/edges increase to 2.75 Å/2.91 Å. A comparison of PI (aluminum doped) and AFI V₂O₃, as based on hard and soft x-ray absorption spectroscopy, revealed the same local symmetry for the metal sites and hence (on a local scale) identical distortions [42].

V_2O_3 is generally regarded as canonical Mott–Hubbard system [27,28]. A description in terms of the one-band Hubbard model is based on a level scheme by Castellani et al. [43]: Crystal field splitting of the V $3d$ states due to the octahedral coordination yields lower t_{2g} and higher e_g^σ states. Because of the trigonal lattice symmetry the former split up into a_{1g} and e_g^π contributions. The non-degenerate a_{1g} orbital points along c_{hex} and gives rise to a one-dimensional band due to covalent bonding. This electronic level scheme was confirmed by band structure calculations [44]. Castellani et al. assumed the bonding a_{1g} orbital as fully occupied, whereas the antibonding states shift energetically above the e_g^π levels. This leaves one electron per vanadium site in the twofold degenerate e_g^π states, making the system susceptible to degeneracy lifting distortions. One e_g^π electron (total spin $S = 1/2$) suggests using the half filled one-band Hubbard model as the simplest model describing V_2O_3 [45].

Experimentally, the PM-AFI phase transition was analyzed by photoelectron spectroscopy. As reported by Shin et al. [33], the spectra show O $2p$ states in the energy range from -10 eV to -4 eV, whereas V $3d$ states occur within 3 eV below the Fermi level. Except for slight modifications of the bandwidth no drastic change is found in the V $3d$ band structure below the MIT. However, the DOS at the Fermi energy is rather small even in the metallic phase. A high resolution photoemission study by Shin et al. [46] revealed a band gap of 0.2 eV for the insulating phase. The PM-PI transition of (chromium doped) V_2O_3 was investigated by Smith and Henrich [47] using photoelectron spectroscopy. In the insulating phase at room temperature they found a low emission intensity at the Fermi level, which increases after cooling into the metallic state. High temperature PI spectra reveal a larger V $3d$ bandwidth than low temperature AFI spectra, which may be due to thermal broadening or absence of magnetic order. According to oxygen K-edge x-ray absorption spectroscopy unoccupied V $3d$ bands extend from 0 eV (Fermi energy) to 6 eV with maxima at about 1 eV and 3 eV [48].

The model of Castellani et al. has been called into question by the results of polarized x-ray absorption spectroscopy, which indicate a vanadium $S = 1$ spin state [49]. Furthermore, the first excited states miss a pure e_g^π symmetry but include a_{1g} contributions, which requires an explanation beyond the pure one-band Hubbard model or beyond models projecting out the a_{1g} states by means of simple dimerization. LDA+U calculations succeeded in explaining the electronic and magnetic properties of the AFI phase, in particular the peculiar antiferromagnetic order [50]. While every vanadium spin is parallel to the adjacent spin along c_{hex} , there are two antiparallel spins and one parallel spin at the nearest in-plane vanadium sites. Enforcing spin degeneracy in the calculation, influence of the crystal structure on the electronic properties was shown to be rather small. Introducing the antiferromagnetic order yields an optical band gap of 0.6 eV. Moreover, LDA+U findings point at a spin $S = 1$ model without orbital degeneracy. In contrast, by means of model calculations Mila et al. [51] proposed a $S = 1$ spin state and orbital degeneracy in the AFI phase. Starting with the assumption of strong covalent bonding in the vanadium pairs along c_{hex} the authors supposed the intersite a_{1g} hopping matrix elements to dominate. However, an analysis of the hopping processes in V_2O_3 revealed hopping integrals between second, third, and fourth nearest vanadium neighbours being equally important for the shape of the a_{1g} band [52]. Evidence for orbital ordering in the AFI phase is taken from magnetic neutron scattering [53].

LDA calculations display only minor response of the electronic structure to crystal parameter changes. But a slight narrowing of the characteristic a_{1g} bands in the insulating phase formed the basis for describing the PM-PI transition by a combination of LDA calculations and the dynamical mean field theory (DMFT), demonstrating the influence of electronic correlations in the insulating phase [54]. Confirming predictions of the LDA+DMFT approach, a prominent quasiparticle peak was observed in the photoemission spectrum of metallic V_2O_3 [55]. However, despite many studies the electronic properties and MITs of V_2O_3 are still controversially discussed. The answer of the electronic states to the structural modifications at the MIT of VO_2 paved the way for interpreting the transition as an embedded Peierls instability. A similar procedure seems to fail for the sesquioxide since here the structural modifications hardly influence the LDA results.

3 Crystal structures of the Magnéli phases: a unified representation

To analyze the electronic properties of the vanadium Magnéli phases, we first have to understand in detail the crystal structures – a prerequisite for relating electronic changes at the MITs of the Magnéli phases to structural transformations occurring simultaneously. We elaborate a new and unifying point of view of the atomic arrangements underlying all members of the series. A distinct advantage of this representation is its applicability to the crystal structures of vanadium dioxide and sesquioxide as well. Thus a comprehensive understanding of the whole Magnéli series V_nO_{2n-1} including its end members VO_2 ($n \rightarrow \infty$) and V_2O_3 ($n = 2$) is eventually achieved. The detailed modifications of the various crystal structures at the MITs are discussed in subsequent sections.

As mentioned before and as is obvious from the stoichiometric relation (1), the crystal structures of the Magnéli phases are usually interpreted as rutile-type slabs separated by shear planes with a corundum-type atomic arrangement [5]. The rutile-type slabs extend infinitely in two dimensions and have a characteristic finite width corresponding to n VO_6 octahedra in the case of the compound V_nO_{2n-1} . Since octahedra at a slab-surface share faces with octahedra from a neighbouring slab, the atomic arrangement at the boundary is closely related to the corundum structure. The rutile crystal structure is therefore disturbed and adjacent slabs are mutually out of phase, thus giving rise to the denotation shear plane. Precise investigation of the changes of the local atomic coordination on passing through the Magnéli series is rather complicated using the ordinary representation of the crystal structures. Thus it is advantageous to describe the structures in a different manner. For that purpose we start with the oxygen sublattice, which turns out to be most similar for all the compounds. As demonstrated for VO_2 and V_2O_3 the sublattice can be understood as a regular space filling network of neighbouring oxygen octahedra. The octahedra are mutually connected via edges along c_{prut} and via faces along $a_{\text{prut}}/b_{\text{prut}}$. In order to illustrate this geometrical arrangement schematical projections (parallel to a_{prut}) of sandwich-like O-V-O slabs cut out of the crystal structures of the dioxide and the sesquioxide are shown in figure 5. A sandwich-like slab consists of a vanadium layer confined by oxygen layers at both ends. Due to the projection the oxygen octahedra appear as hexagonal structures and the octahedral network becomes a two-dimensional hexagonal network.

Both the infinite vanadium chains of VO_2 (along c_{prut}) and the hexagonal arrangement of the vanadium atoms in V_2O_3 are clearly visible in figure 5. Actually, the basic structural features of the dioxide and the sesquioxide are captured completely in this graphical representation. Adjacent slabs yield the same projection as shown except for a possible translation perpendicular to a_{prut} . To be more specific, in adjacent VO_2 slabs filled and empty oxygen octahedra, i.e. filled and empty oxygen hexagons, are interchanged. In neighbouring V_2O_3 slabs the vanadium atoms are shifted by one hexagon along the c_{prut} -direction. To sum up, provided that the oxygen networks of VO_2 and V_2O_3 are exactly the same, the only difference between the compounds arises from a different vanadium sublattice. The configuration of the latter is optimally described in terms of the presented slab-type projection. In particular, the infinite vanadium chains belonging to the dioxide are contrasted with finite chains of length 2 in the case of the sesquioxide. Such a description of the V_2O_3 structure in terms of 2-chains along c_{prut} instead of hexagonal arrangements is preferable for a systematic discussion. There are small differences between the oxygen sublattices of VO_2 and V_2O_3 . However, they do not affect the gross features of the oxygen arrangement, but still are essential for a detailed comparison of the materials. As indicated by our representation in terms of O-V-O slabs we find alternating vanadium and oxygen layers along a_{prut} in both compounds. While the oxygen layers of the sesquioxide are almost flat, we are confronted with a distinct buckling in the case of the dioxide, which is caused by an elongated apical V-O distance. The buckling of the oxygen layers is associated with the fact that octahedral faces oriented perpendicular to a_{prut} in V_2O_3 adopt a tilt in the VO_2 case. Nonetheless, the characteristic feature distinguishing vanadium dioxide and sesquioxide certainly is their different pattern of filling the oxygen network with vanadium atoms.

Having developed a common description for the crystal structures of the end members of the Magnéli series it is easy to extend this point of view to the remaining compounds. For that purpose the structures of V_4O_7 and V_6O_{11} are depicted in figure 6 analogous with the representations of VO_2 and V_2O_3 in figure

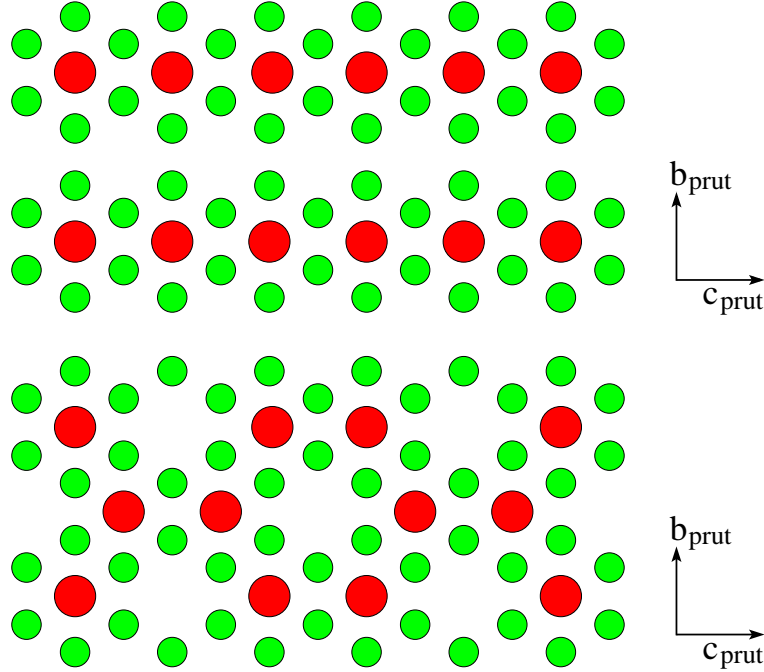


Fig. 5 Projection parallel to a_{prut} of a O-V-O sandwich-like slab cut out of the crystal structures of VO_2 (top) and V_2O_3 (bottom). Large and small spheres represent vanadium and oxygen atoms, respectively. Due to the projection the oxygen octahedra form a regular hexagonal network. For VO_2 infinite chains of vanadium atoms run along the pseudorutile c_{prut} -axis, where the oxygen octahedra are connected by common edges. The projection of an adjacent O-V-O slab results in a similar configuration – but empty and filled octahedra are exchanged. Thus the metal atoms in VO_2 lack nearest neighbours in the a_{prut} -direction. For V_2O_3 finite chains of two vanadium atoms run along the c_{prut} -axis. The projection of an adjacent O-V-O slab reveals a shift by one octahedral site along c_{prut} . As a consequence, the vanadium atoms exhibit exactly one nearest vanadium neighbour in the a_{prut} -direction.

5. Except for a slightly different buckling of the oxygen layers, which is visible in figure 7 for V_4O_7 , the aforementioned regular three-dimensional oxygen network forms the basis of all Magnéli phases. Hence the hexagonal arrangement of the oxygen atoms in the projection of the O-V-O sandwich-like slabs does not change. In contrast, each particular material is characterized by the way of filling the oxygen network with vanadium atoms. Obviously, there are chains of vanadium atoms running along the c_{prut} -axis, which comprise four and six atoms in the case of V_4O_7 and V_6O_{11} , respectively. In general, there are vanadium chains of length n in V_nO_{2n-1} . Looking back to the dioxide ($n = \infty$) and the sesquioxide ($n = 2$) this rule coincides with our finding of infinite chains and 2-chains, respectively. In a particular compound all metal chains reveal the same length, defined by the parameter n ; $n - 1$ empty oxygen octahedra separate them in the c_{prut} -direction. Vanadium chains neighbouring along b_{prut} overlap by roughly half the in-chain V-V distance, thus giving rise to the characteristic chain end arrangement depicted in figure 6. This chain end configuration is conserved in the whole Magnéli series and only the length of the chain center changes. For VO_2 there are actually no chain ends and the 2-chains of V_2O_3 contain no center atom.

The atomic arrangement represented by the projections of the O-V-O slabs is unaltered for slabs neighbouring in the a_{prut} -direction. Only the vanadium sublattice is shifted along the c_{prut} -axis by an amount of $n - 1$ octahedral sites, i.e. $n - 1$ hexagons in the sandwich-like projection. Thus the last vanadium atom of a metal chain is seated on top of the first atom of a chain in the adjacent slab, see figures 8 and 9. Hence the chain end atoms exhibit exactly one nearest vanadium neighbour along the a_{prut} -axis, whereas each chain

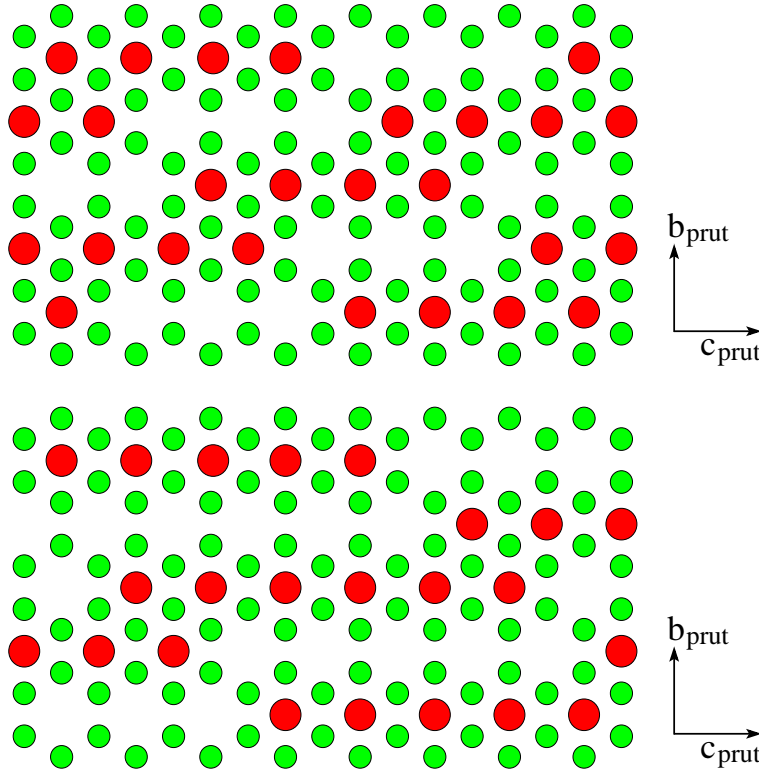


Fig. 6 Projection along a_{prut} of a O-V-O sandwich-like slab from the crystal structures of V_4O_7 (top) and V_6O_{11} (bottom). Large and small spheres represent vanadium and oxygen atoms, respectively. As in the cases of vanadium dioxide and sesquioxide the oxygen octahedra form a regular hexagonal network and the octahedral sites are partially occupied by metal atoms, giving rise to vanadium chains along c_{prut} . The chains consist of $n = 4$ or $n = 6$ atoms, separated by $n - 1 = 3$ or $n - 1 = 5$ empty octahedra. Along b_{prut} the chains overlap by roughly half the intrachain V-V distance. The projection of an adjacent O-V-O slab results in a similar configuration – but the vanadium sublattice is shifted along c_{prut} by $n - 1 = 3$ or $n - 1 = 5$ octahedral sites. As a consequence, chain end atoms exhibit one nearest vanadium neighbour in the a_{prut} -direction, whereas center atoms reveal none.

center atom is surrounded by two empty sites in this direction. All the above considerations apply to each Magnéli compound. Chain center sites hence mirror the local atomic coordination known from VO_2 with nearest vanadium neighbours only in the chain direction. Instead, the coordination of the chain end atoms resembles the crystal structure of V_2O_3 with one nearest vanadium neighbour along a_{prut} and c_{prut} . Due to the varying length of the vanadium chains in a qualitatively unchanged oxygen sublattice, the different Magnéli phases have different stoichiometric V:O ratios reaching from 1:2 in VO_2 to 2:3 in V_2O_3 . As the crystal structures of the Magnéli phases are connected to each other simply by removing or inserting chain center atoms, the Magnéli series allows us to transfer a dioxide-type atomic arrangement step by step into a sesquioxide-type arrangement. Using these systematics we gain insight into the interplay between VO_2 and V_2O_3 -like regions and their effects on the MIT. Taking into account the mixed valent metal states, the Magnéli series transfers the electronic configuration of the dioxide (d^1) into that of the sesquioxide (d^2).

In the following sections two particular Magnéli phases are discussed in detail: V_4O_7 and V_6O_{11} . To define the notation of the different metal sites figure 8 gives a schematic view of the V_4O_7 crystal structure where the regular network of oxygen octahedra has not been included for simplicity. We identify vanadium 4-chains parallel to the c_{prut} -direction. Due to mutual interconnection of the chains along a_{prut} a kind of

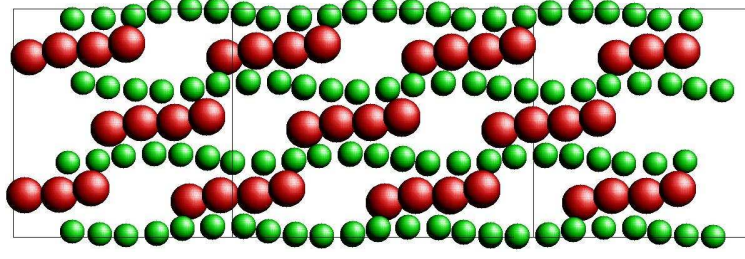


Fig. 7 Vanadium (large) and oxygen (small) layers in the case of the V_4O_7 crystal structure, projection perpendicular to a_{prut} . A distinct buckling of the oxygen layers is clearly visible.

stair-like vanadium arrangement is observable. Stair endings resemble the corundum atomic coordination (figure 4), whereas intermediate plateaus are due to the rutile regions of the crystal. The longer the central part of the vanadium chains, the larger the separation of the stair endings and the dioxide-like character of the crystal. The illustration of V_6O_{11} in figure 9 is different from figure 8 due to longer vanadium chains. We find four crystallographically inequivalent vanadium sites in the case of V_4O_7 and six sites for V_6O_{11} . In both structures these sites set up two types of metal chains: for V_4O_7 we find the series V1-V3-V3-V1 and V2-V4-V4-V2, whereas for V_6O_{11} the series V1-V3-V5-V5-V3-V1 and V2-V4-V6-V6-V4-V2 arise. Vanadium layers comprising either chains of the first or of the second kind alternate along a_{prut} .

The V-V distances given as insets in the above figures address the dominating structural changes accompanying the MIT of both V_4O_7 and V_6O_{11} [57–60]. At the phase transition of the former compound the dimerization in the 1-3 chains becomes stronger and an additional dimerization evolves in the 2-4 chains. Thereby the dimerization patterns are reversed because the longer V-V distance appears at the chain ends and the chain center, respectively. The V1-V2 bond length is almost constant. For V_6O_{11} changes in the 1-3-5 chains are small although a little dimerization is present at low temperatures. In contrast, the 2-4-6 chains evolve a pronounced dimerization at the transition. Again the variation of the V1-V2 bond length is by far the smallest observed. A profound analysis of the structural changes induced by the MITs is given in the subsequent sections where we relate LDA results to local structural properties. However, signatures of the VO_2 -like dimerization are reflected by both V_4O_7 and V_6O_{11} .

As far as the question of choosing the unit cells of the Magnéli phases is concerned, several definitions have been used in the literature. Andersson and Jahnberg [5] defined primitive translations in terms of the rutile lattice $(\mathbf{a}_A, \mathbf{b}_A, \mathbf{c}_A) = M(\mathbf{a}_R, \mathbf{b}_R, \mathbf{c}_R)$, where they distinguished the cases n odd and n even

$$M_{\text{odd}} = \begin{pmatrix} -1 & 0 & 1 \\ 1 & 1 & 1 \\ \frac{n-3}{2} & \frac{2-n}{2} & \frac{6-n}{2} \end{pmatrix}, \quad M_{\text{even}} = \begin{pmatrix} -1 & 0 & 1 \\ 1 & 1 & 1 \\ n-3 & 2-n & 6-n \end{pmatrix}. \quad (2)$$

However, this proposal is not useful for a comparison within the Magnéli series since for every parameter value n the vanadium chains extend in different directions of the unit cell, and due to the two families of cell parameters. Le Page and Strobel [61] hence proposed an alternative set of primitive translations with the c -axis parallel to the vanadium chains

$$\begin{pmatrix} \mathbf{a}_L \\ \mathbf{b}_L \\ \mathbf{c}_L \end{pmatrix} = \begin{pmatrix} -1 & 0 & 1 \\ 1 & 1 & 1 \\ 0 & 0 & 2n-1 \end{pmatrix} \begin{pmatrix} \mathbf{a}_R \\ \mathbf{b}_R \\ \mathbf{c}_R \end{pmatrix}. \quad (3)$$

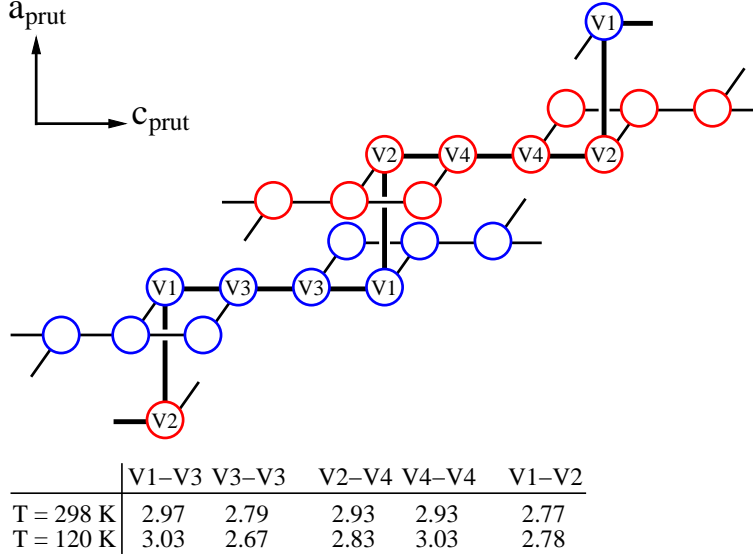


Fig. 8 Crystal structure of V_4O_7 . For simplicity this schematic view does not include the oxygen sublattice. The metal atoms form chains of length $n = 4$ along c_{prut} . There are 4 inequivalent sites in the chains V1-V3-V3-V1 and V2-V4-V4-V2. Layers perpendicular to a_{prut} either comprise chains of the first or of the second kind. The table gives measured V-V distances (in Å) for both the metallic (298 K) and insulating (120 K) phase of V_4O_7 [59].

While the unit cell of Andersson and Jahnberg is A-centered, the cell of Le Page and Strobel is I-centered. Finally, Horiuchi et al. [62] introduced a primitive unit cell with translation vectors

$$\begin{pmatrix} \mathbf{a}_H \\ \mathbf{b}_H \\ \mathbf{c}_H \end{pmatrix} = \begin{pmatrix} -1 & 0 & 1 \\ 1 & 1 & 1 \\ 0 & n - \frac{1}{2} & n - \frac{1}{2} \end{pmatrix} \begin{pmatrix} \mathbf{a}_R \\ \mathbf{b}_R \\ \mathbf{c}_R \end{pmatrix}. \quad (4)$$

Because this unit cell has half the size than the previous cells we adopt it for our calculation. Application of relation (4) based on the parent rutile lattice is feasible whenever the crystal symmetry is triclinic with space group $P\bar{1}$ (C_i^1) [63], which is the case for the Magnéli compounds with parameters $n = 4, \dots, 9$. In contrast, V_3O_5 crystallizes in a body-centered and simple monoclinic lattice with space group $I2/c$ (C_{2h}^6) and $P2_1/c$ (C_{2h}^4) above and below the MIT, respectively [64, 65].

4 Structural and calculational details

The first vanadium Magnéli compound we discuss at length is V_6O_{11} , see section 5. In doing so we can benefit from a suitable application of the knowledge we already acquired by our former considerations of VO_2 . Consequently, it is convenient to choose V_6O_{11} as the starting point of a comprehensive analysis of the whole Magnéli class. Similar to the MIT of vanadium dioxide and the PM-AFI transition of vanadium sesquioxide, the MIT of V_6O_{11} at 170 K is accompanied by distinct structural transformation. According to an x-ray study by Canfield [60], V_6O_{11} crystallizes in a triclinic lattice with space group $P\bar{1}$ (C_i^1). The vanadium and oxygen atoms are located at the Wyckoff positions (2i): $\pm(x, y, z)$. For the triclinic lattice parameters the author reported $a_L = 5.449$ Å, $b_L = 7.010$ Å, $c_L = 31.437$ Å, $\alpha_L = 67.15^\circ$, $\beta_L = 57.45^\circ$, and $\gamma_L = 108.90^\circ$ at 298 K. Below the phase transition (at 20 K) he found the parameters $a_L = 5.495$ Å, $b_L = 6.944$ Å, $c_L = 31.484$ Å, $\alpha_L = 67.40^\circ$, $\beta_L = 57.13^\circ$, and $\gamma_L = 108.61^\circ$. These values are related to the unit cell of Le Page and Strobel as denoted in equation (3), where $n = 6$. The primitive translations

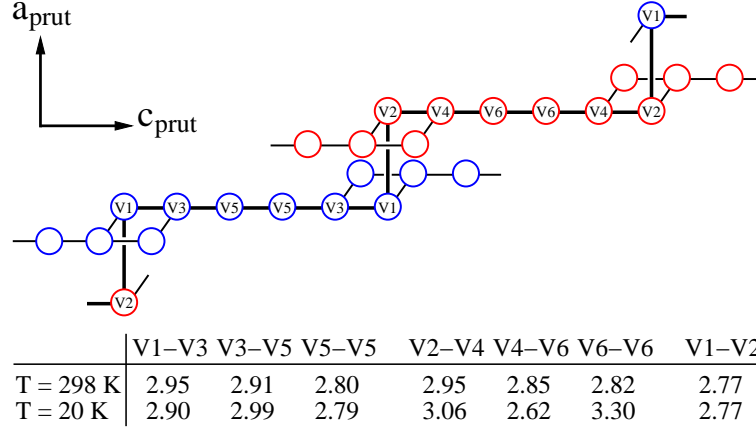


Fig. 9 Crystal structure of V_6O_{11} . For simplicity this schematic view does not include the oxygen sublattice. The metal atoms form chains of length $n = 6$ along c_{prut} . There are 6 inequivalent sites in the chains V1-V3-V5-V5-V3-V1 and V2-V4-V6-V6-V4-V2. Layers perpendicular to a_{prut} either comprise chains of the first or of the second kind. The table gives measured V-V distances (in Å) for both the metallic (298 K) and insulating (20 K) phase of V_6O_{11} [60].

of Horiuchi et al. take the form

$$\begin{pmatrix} \mathbf{a}_H \\ \mathbf{b}_H \\ \mathbf{c}_H \end{pmatrix} = \begin{pmatrix} -1 & 0 & 1 \\ 1 & 1 & 1 \\ 0 & \frac{11}{2} & \frac{11}{2} \end{pmatrix} \begin{pmatrix} \mathbf{a}_R \\ \mathbf{b}_R \\ \mathbf{c}_R \end{pmatrix} = \begin{pmatrix} 1 & 0 & 0 \\ 0 & 1 & 0 \\ \frac{11}{2} & \frac{11}{2} & -\frac{1}{2} \end{pmatrix} \begin{pmatrix} \mathbf{a}_L \\ \mathbf{b}_L \\ \mathbf{c}_L \end{pmatrix} \quad (5)$$

and coordinates given in the L -system can directly be transformed into the H -system

$$\begin{pmatrix} x \\ y \\ z \end{pmatrix}_H = \begin{pmatrix} 1 & 0 & 11 \\ 0 & 1 & 11 \\ 0 & 0 & -2 \end{pmatrix} \begin{pmatrix} x \\ y \\ z \end{pmatrix}_L + \begin{pmatrix} 1/2 \\ 0 \\ 1/2 \end{pmatrix}_L. \quad (6)$$

The translation vector has to be added because of different choices of the origin in both coordinate systems. With the help of equation (6) the positional parameters reported by Canfield for both the high and the low temperature configuration of V_6O_{11} yield the structural input for the band structure calculation, which is summarized in table 2. In addition to the six inequivalent vanadium atoms there are eleven oxygen sites. Due to the inversion symmetry of the crystal lattice the unit cell contains 34 atoms. Further structural data for metallic V_6O_{11} were given by Horiuchi et al. [62]. However, we use the data of Canfield.

To allow for an adequate interpretation of the electronic structure results, it is important to preserve close relation between the representation of the V_6O_{11} structure and the parent rutile structure. We arrange the unit cell of the L -system in a Cartesian coordinate system such that the alignment of the oxygen octahedra resembles the rutile arrangement; we assume $\mathbf{a}_L = (-a_1, 0, a_3)$, $\mathbf{b}_L = (a_1, b_2, a_3)$, and $\mathbf{c}_L = (c_1, c_2, c_3)$. An application of the elementary relations $a_L^2 = a_1^2 + a_3^2$, $b_L^2 = a_1^2 + b_2^2 + a_3^2$, and $\mathbf{a}_L \cdot \mathbf{b}_L = a_L b_L \cos \gamma_L$ immediately yields $a_{1/3}^2 = 1/2 \cdot (a_L^2 \mp a_L b_L \cos \gamma_L)$ and $b_2^2 = a_L^2 - a_{1/3}^2$. Furthermore, from the expressions $\mathbf{a}_L \cdot \mathbf{c}_L = a_L c_L \cos \beta_L$ as well as $\mathbf{b}_L \cdot \mathbf{c}_L = b_L c_L \cos \alpha_L$ one finds $c_{1/3} = (b_L c_L \cos \alpha_L \mp a_L c_L \cos \beta_L - b_2 c_2)/2a_{1/3}$, which implies a quadratic equation for c_2 because $c_L^2 = c_1^2 + c_2^2 + c_3^2$. Solving this equation completes the calculation of the unit cell in the L -system and a transformation via equation (5) yields the unit cell in the H -system. For the high temperature structure of V_6O_{11} at 298 K we find ($A = 8.6665 a_B$)

$$\mathbf{a}_H = A \begin{pmatrix} -1.0000 \\ 0.0000 \\ 0.6417 \end{pmatrix}, \quad \mathbf{b}_H = A \begin{pmatrix} 1.0000 \\ 0.9616 \\ 0.6417 \end{pmatrix}, \quad \mathbf{c}_H = A \begin{pmatrix} -0.0053 \\ 5.4629 \\ 3.6352 \end{pmatrix}. \quad (7)$$

Atom	High temperature structure			Low temperature structure		
	x	y	z	x	y	z
V1	0.9931	0.4467	0.0624	0.9986	0.4633	0.0584
V2	0.9731	0.9264	0.0672	0.0081	0.9568	0.0612
V3	0.9652	0.4583	0.2422	0.9578	0.4379	0.2506
V4	0.9560	0.9463	0.2432	0.9362	0.9362	0.2484
V5	0.9765	0.4689	0.4170	0.9885	0.5086	0.4074
V6	0.9823	0.9777	0.4152	0.0582	0.0473	0.4036
O1	0.6888	0.4114	0.0332	0.6584	0.3744	0.0402
O2	0.3202	0.5570	0.0666	0.3173	0.5650	0.0658
O3	0.6845	0.4670	0.1090	0.6809	0.4685	0.1098
O4	0.3736	0.6180	0.1460	0.3464	0.5937	0.1508
O5	0.6930	0.4060	0.2134	0.6954	0.4057	0.2150
O6	0.3138	0.5883	0.2468	0.3360	0.6176	0.2396
O7	0.6697	0.4485	0.2968	0.6683	0.4469	0.2974
O8	0.3171	0.5339	0.3474	0.3161	0.5435	0.3468
O9	0.7039	0.4223	0.3898	0.6826	0.3998	0.3940
O10	0.3180	0.5976	0.4254	0.3510	0.6150	0.4224
O11	0.6864	0.4689	0.4718	0.6983	0.4710	0.4704

Table 2 Atomic positions for the high and low temperature structure of V_6O_{11} as used in the band structure calculations. These data have been determined by Canfield [60]; the coordinates refer to the primitive translations proposed by Horiuchi et al. [62].

The low temperature structure at 20 K results in ($A = 8.6981 a_B$)

$$\mathbf{a}_H = A \begin{pmatrix} -1.0000 \\ 0.0000 \\ 0.6521 \end{pmatrix}, \quad \mathbf{b}_H = A \begin{pmatrix} 1.0000 \\ 0.9224 \\ 0.6521 \end{pmatrix}, \quad \mathbf{c}_H = A \begin{pmatrix} -0.0074 \\ 5.3417 \\ 3.7636 \end{pmatrix}. \quad (8)$$

The Bohr radius is denoted by a_B and the primitive translations refer to Cartesian coordinates. The corresponding positional parameters of the vanadium and oxygen atoms are denoted in table 2.

The presented LDA calculations are based on the (scalar relativistic) augmented spherical wave (ASW) method [66, 67]. We adopt the parametrization of the exchange correlation potential introduced by Vosko, Wilk, and Nusair [68]. The ASW scheme uses the atomic sphere approximation and models the full crystal potential by means of spherical symmetric potential wells. Here it is required that the atomic spheres fill the space of the unit cell. For open crystal structures problems can arise because space filling only due to atom centered spheres may lead to large overlap. As a consequence, so-called empty spheres, i.e. pseudo atoms without nuclei, have to be introduced. They are used to correctly model the shape of the crystal potential in large voids. The collection of both physical and empty spheres leads to an artificial close-packed structure. However, since the potential of the whole set of spheres ought to represent the crystal potential as exactly as possible it is a challenge to find optimal empty sphere positions and optimal radii for the real and empty spheres. Here the sphere geometry optimization algorithm described in [69] is most efficient.

By adding 35 empty spheres from 18 crystallographically inequivalent classes to the triclinic unit cell of high temperature V_6O_{11} it is possible to keep the linear overlap of real spheres below 18%. Simultaneously, the overlap of any pair of real and empty spheres is smaller than 23%. In the case of the low temperature structure 40 empty spheres from 21 inequivalent classes allow for reducing the overlaps to less than 18% and 23%, respectively. Summing up, the unit cell entering the LDA calculation comprises 69 spheres for the high and 74 spheres in the case of the low temperature structure. The radii of the vanadium and oxygen spheres are summarized in table 3, which additionally denotes the valence charges arising from the LDA

Atom	High temperature structure		Low temperature structure	
	Radius	Charge	Radius	Charge
V1	2.1866	2.5090	2.2303	2.6179
V2	2.1587	2.7155	2.2278	2.8276
V3	2.2833	2.5240	2.2158	2.5534
V4	2.2755	2.7564	2.2248	2.7939
V5	2.3440	2.7775	2.2248	2.5213
V6	2.3437	2.7354	2.1856	2.6201
O1	1.9684	4.1741	1.9423	4.2072
O2	1.7883	4.0164	1.8240	3.9466
O3	1.9680	4.3682	1.9699	4.4187
O4	2.0093	4.3624	1.9420	4.2381
O5	1.7654	3.8853	1.8219	3.8832
O6	1.8752	4.0164	1.8201	3.9683
O7	1.8673	4.0673	1.7943	3.9711
O8	1.8908	4.0278	1.8394	4.0294
O9	1.8585	4.0833	1.8568	4.0498
O10	1.8828	4.1106	1.8121	3.9479
O11	1.9170	4.0959	1.8166	3.8850

Table 3 Radii of the vanadium/oxygen spheres (in a_B) as well as calculated LDA valence charges (V $3d$ or O $2p$) for both the high and the low temperature phase of V_6O_{11} .

band structure calculation. For both V_6O_{11} structures the basis sets taken into account in the secular matrix comprise V $4s$, $4p$, $3d$, ($4f$) and O $2s$, $2p$, ($3d$) orbitals. States given in parentheses enter as tails of other states; for details on the ASW method see [67, 70]. To complete the basis sets we add empty sphere states, which are determined with respect to the spacial extensions of the spheres and the total charge occupying them. The used configurations reach from $1s$, ($2p$) to $1s$, $2p$, $3d$, $4f$, ($5g$). During the course of the LDA calculation the Brillouin zone is sampled with an increasing number of \mathbf{k} -points in the irreducible wedge. In this manner one ensures convergence of the results with respect to the fineness of the \mathbf{k} -space grid. For both the high and low temperature calculation the number of \mathbf{k} -points was increased from 108 to 256, 864, and 2048. Self-consistency of the charge density was assumed for deviations of the atomic charges and the total energy of subsequent iterations less than 10^{-8} electrons and 10^{-8} Ryd, respectively.

As V_4O_7 reveals short metal chains (length $n = 4$) it is suitable for investigating the electronic features of the sesquioxide-like chain end sites and their influence on the MIT. Using our results for V_6O_{11} we can understand the MIT of V_4O_7 . Afterwards we establish important implications for the frequently discussed MITs of V_2O_3 . As for V_6O_{11} , the space group of V_4O_7 is $P\bar{1}$ (C_i^1) and the MIT at 250 K is accompanied by a structural distortion. Refinements tracing back to Hodeau and Marezio [59] placed the vanadium and oxygen sites at the Wyckoff positions (2i): $\pm(x, y, z)$. Above the transition at 298 K the authors observed the triclinic parameters $a_A = 5.509 \text{ \AA}$, $b_A = 7.008 \text{ \AA}$, $c_A = 12.256 \text{ \AA}$, $\alpha_A = 95.10^\circ$, $\beta_A = 95.17^\circ$, and $\gamma_A = 109.25^\circ$. The corresponding values at low temperatures (120 K) are $a_A = 5.503 \text{ \AA}$, $b_A = 6.997 \text{ \AA}$, $c_A = 12.256 \text{ \AA}$, $\alpha_A = 94.86^\circ$, $\beta_A = 95.17^\circ$, and $\gamma_A = 109.39^\circ$. This refers to the unit cell of Andersson and Jahnberg, see equation (2) with $n = 4$. The primitive translations of Horiuchi et al. are given by

$$\begin{pmatrix} \mathbf{a}_H \\ \mathbf{b}_H \\ \mathbf{c}_H \end{pmatrix} = \begin{pmatrix} -1 & 0 & 1 \\ 1 & 1 & 1 \\ 0 & \frac{7}{2} & \frac{7}{2} \end{pmatrix} \begin{pmatrix} \mathbf{a}_R \\ \mathbf{b}_R \\ \mathbf{c}_R \end{pmatrix} = \begin{pmatrix} 1 & 0 & 0 \\ 0 & 1 & 0 \\ 2 & \frac{5}{2} & -\frac{1}{2} \end{pmatrix} \begin{pmatrix} \mathbf{a}_A \\ \mathbf{b}_A \\ \mathbf{c}_A \end{pmatrix} \quad (9)$$

Atom	High temperature structure			Low temperature structure		
	x	y	z	x	y	z
V1	0.9806	0.9383	0.1008	0.9773	0.9299	0.1043
V2	0.9946	0.4509	0.0964	0.9781	0.4382	0.1008
V3	0.9662	0.9613	0.3742	0.9508	0.9512	0.3757
V4	0.9914	0.4905	0.3658	0.0146	0.5021	0.3608
O1	0.6927	0.4137	0.0514	0.6932	0.4151	0.0512
O2	0.3237	0.5551	0.1036	0.3191	0.5383	0.1112
O3	0.6825	0.4643	0.1716	0.6808	0.4658	0.1718
O4	0.3763	0.6232	0.2254	0.3804	0.6214	0.2254
O5	0.6893	0.4112	0.3328	0.7018	0.4240	0.3278
O6	0.3044	0.5683	0.3910	0.2793	0.5257	0.4068
O7	0.6605	0.4326	0.4700	0.6616	0.4218	0.4728

Table 4 Atomic positions for the high and low temperature structure of V_4O_7 as used in the band structure calculations. These data trace back to Hodeau and Marezio [59]; the coordinates refer to the primitive translations proposed by Horiuchi et al. [62].

and we are able to transform coordinates from the A -system into the H -system

$$\begin{pmatrix} x \\ y \\ z \end{pmatrix}_H = \begin{pmatrix} 1 & 0 & 4 \\ 0 & 1 & 5 \\ 0 & 0 & -2 \end{pmatrix} \begin{pmatrix} x \\ y \\ z \end{pmatrix}_A + \begin{pmatrix} 1/2 \\ 1/2 \\ 1/2 \end{pmatrix}. \quad (10)$$

Again, the translation vector has been added to account for different choices of the origin in the coordinate systems. Using equation (10) the positional parameters of Hodeau and Marezio for high and low temperature V_4O_7 result in the values summarized in table 4, which enter the LDA calculation. Alternative data for the crystal structure were given by Horiuchi et al. [57] and Marezio et al. [58]. Altogether, one obtains four crystallographically inequivalent vanadium and seven oxygen sites. Due to the inversion symmetry of the lattice the V_4O_7 unit cell contains 22 atoms.

Using the lattice constants of Hodeau and Marezio we set up the triclinic unit cell of V_4O_7 in Cartesian coordinates. Because of the similar definitions of the A and L -system we can proceed analogous with our considerations for V_6O_{11} , applying the parameters a_A , b_A , c_A , α_A , β_A and γ_A . Via equation (9) we find a unit cell in the H -system. For the high temperature structure at 298 K this yields ($A = 8.7702 a_B$)

$$\mathbf{a}_H = A \begin{pmatrix} -1.0000 \\ 0.0000 \\ 0.6396 \end{pmatrix}, \quad \mathbf{b}_H = A \begin{pmatrix} 1.0000 \\ 0.9333 \\ 0.6396 \end{pmatrix}, \quad \mathbf{c}_H = A \begin{pmatrix} 0.0071 \\ 3.4280 \\ 2.3282 \end{pmatrix}. \quad (11)$$

Moreover, the low temperature configuration at 120 K results in ($A = 8.7691 a_B$)

$$\mathbf{a}_H = A \begin{pmatrix} -1.0000 \\ 0.0000 \\ 0.6374 \end{pmatrix}, \quad \mathbf{b}_H = A \begin{pmatrix} 1.0000 \\ 0.9313 \\ 0.6374 \end{pmatrix}, \quad \mathbf{c}_H = A \begin{pmatrix} 0.0054 \\ 3.4199 \\ 2.3141 \end{pmatrix}. \quad (12)$$

These primitive translations are used with the positional parameters denoted in table 4.

Similar to the procedure in the case of V_6O_{11} we insert additional augmentation spheres into the V_4O_7 structure to account for its openness and to properly model the crystal potential. For both the high and the low temperature phase it suffices to apply 13 crystallographically inequivalent classes and place altogether 24 empty spheres in the triclinic unit cell. This keeps the linear overlap of physical spheres below 19% and the overlap of any pair of physical and empty spheres below 24%. Unit cells entering the LDA calculation

Atom	High temperature structure		Low temperature structure	
	Radius	Charge	Radius	Charge
V1	2.2002	2.7937	2.1388	2.7457
V2	2.2349	2.6572	2.3468	2.7529
V3	2.3224	2.7329	2.1999	2.7430
V4	2.3433	2.7245	2.3436	2.6778
O1	1.9931	4.3397	2.0096	4.3259
O2	1.8278	4.0266	1.9267	4.1770
O3	1.9883	4.4309	1.9759	4.4115
O4	2.0465	4.3530	2.0226	4.3440
O5	1.7994	3.9182	1.7492	3.8328
O6	1.8993	4.0359	1.8357	3.9669
O7	1.9164	4.1097	1.9045	4.0616

Table 5 Radii of the vanadium/oxygen spheres (in a_B) as well as calculated LDA valence charges (V 3d or O 2p) for both the high and the low temperature phase of V_4O_7 .

comprise 46 spheres; table 5 denotes the radii of the physical spheres and the calculated valence charges. All technical details of the calculation are the same as for V_6O_{11} .

By comparing V_7O_{13} to V_8O_{15} the influence of the chain center atoms on the electronic properties of the Magnéli phases will be investigated quantitatively in section 7. Such a comparison is of special interest since the former compound is the only member of the Magnéli series, which does not undergo an MIT. In contrast, V_8O_{15} exhibits an MIT at ≈ 70 K accompanied by structural distortions. V_7O_{13} and both V_8O_{15} phases crystallize in the triclinic space group $P\bar{1}$ (C_i^1) with the vanadium and oxygen atoms at the Wyckoff positions (2i): $\pm(x, y, z)$. Canfield [60] reported lattice parameters related to the unit cell of Le Page and Strobel, see equation (3). For V_7O_{13} we have $a_L = 5.439 \text{ \AA}$, $b_L = 7.013 \text{ \AA}$, $c_L = 37.161 \text{ \AA}$, $\alpha_L = 67.04^\circ$, $\beta_L = 57.46^\circ$, and $\gamma_L = 108.92^\circ$. For the room temperature structure of V_8O_{15} these constants amount to $a_L = 5.431 \text{ \AA}$, $b_L = 7.017 \text{ \AA}$, $c_L = 42.896 \text{ \AA}$, $\alpha_L = 66.84^\circ$, $\beta_L = 57.55^\circ$, and $\gamma_L = 108.94^\circ$, whereas the low temperature configuration is defined by the values $a_L = 10.892 \text{ \AA}$, $b_L = 6.980 \text{ \AA}$, $c_L = 85.907 \text{ \AA}$, $\alpha_L = 66.83^\circ$, $\beta_L = 57.38^\circ$, and $\gamma_L = 108.67^\circ$. The latter unit cell is exceptional because it accounts for a superstructure evolving in V_8O_{15} at low temperatures, which complicates the considerations. However, for the high temperature structures we proceed analogous with the previous analysis of V_6O_{11} . A detailed discussion of the structural input for the subsequently presented electronic structure calculations has been given in [71]. We use the positional parameters measured by Canfield. Alternative crystallographic studies of V_7O_{13} at room temperature were performed by Horiuchi et al. [62].

5 Dimerization and localization in V_6O_{11}

In this section we analyze the MIT of V_6O_{11} [72]. Changes of the electronic structure at the transition are discussed in relation to the structural transformations occurring simultaneously. The study will benefit from our unified representation of the crystal structures of the Magnéli phases as well as of VO_2 and V_2O_3 . We will succeed in grouping the electronic bands of V_6O_{11} into states behaving similarly to either the dioxide or the sesquioxide. Therefore it is possible to analyze the phase transitions of the different compounds on the basis of a common point of view, which helps us to gain insight into the delicate interplay of electron-lattice coupling and electronic correlations and their influence on the respective MITs.

We start our considerations with a survey of the partial densities of states shown in figure 10, which arise from the LDA calculations for high and low temperature V_6O_{11} . The low temperature antiferromagnetism is not considered for the reasons discussed earlier. In the high temperature case we observe three groups of bands in the energy intervals from -8.2 eV to -2.9 eV , from -0.7 eV to 1.8 eV , and from 2.0 eV to 4.8 eV .

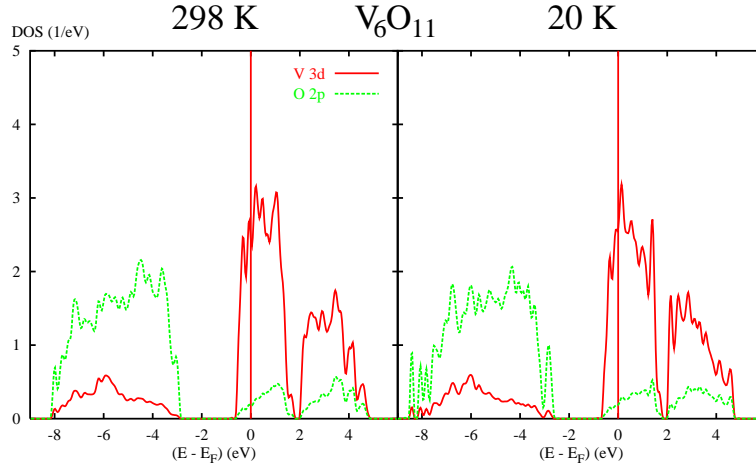


Fig. 10 Partial V 3d and O 2p densities of states (DOS) per vanadium atom resulting from the high (298 K) and low (20 K) temperature crystal structure of V_6O_{11} are compared.

On entering the low temperature phase the lowest group broadens considerably, reaching from -8.4 eV to -2.7 eV, whereas the other groups are almost not altered. Due to substantial structural similarities to the dioxide/sesquioxide it is not surprising that the electronic structure of V_6O_{11} resembles the expectations of the molecular orbital picture as discussed for the former compounds. Characteristic σ and π -type overlap of V 3d and O 2p states gives rise to bonding-antibonding split molecular orbitals in the energetical order σ - π - π^* - σ^* . Bonding states are identified with the lowest, π^* states with the middle, and σ^* states with the highest group of bands. Since the metal atoms are octahedrally coordinated, the σ^* and π^* bands display e_g^{σ} and t_{2g} symmetry, respectively. Because of 12 V and 22 O atoms per unit cell there are $12 \times 2 = 24$ vanadium 3d e_g^{σ} , $12 \times 3 = 36$ vanadium 3d t_{2g} , and $22 \times 3 = 66$ oxygen 2p bands. In agreement with the molecular orbital picture and the findings for VO_2 and V_2O_3 the energetically lowest structure in figure 10 predominantly traces back to O 2p states, whereas the other groups mainly originate from V 3d states. Due to a different electron count, the filling of the t_{2g} levels is between that of VO_2 and V_2O_3 . Contributions of vanadium and oxygen in regions dominated by the respective other states are due to p - d hybridization. In regions corresponding to σ -type V-O overlap, i.e. in the e_g^{σ} range and in the lower half of the O 2p range, they are stronger. Larger t_{2g} admixtures in the e_g^{σ} interval of V_6O_{11} , compared to VO_2 , point to increased deviations from an ideal octahedral coordination. The distortions agree more with those of V_2O_3 .

Differences between the partial densities of states calculated for the high and low temperature structure are small. No energy gap is observed for the low temperature structure. Instead, the structural modifications accompanying the MIT leave the DOS at the Fermi energy almost unaffected. This is not surprising as for neither the insulating phase of VO_2 nor the AFI phase of V_2O_3 did the calculations succeed in reproducing an energy gap, which fact was attributed to shortcomings of the LDA. However, as has been demonstrated for the dioxide, this does not prevent us from understanding the mechanism of the MIT [24, 36]. Since we study the relations between electronic states and local atomic environments as well as the modification of this relationship at the transition, the LDA limitations do not affect the following considerations.

The structural modifications of V_6O_{11} at 170 K are mainly concerned with a strong V4-V6 dimerization in the 2-4-6 vanadium chain, see figure 9. While the V4-V6 bond length decreases from 2.85 Å to 2.62 Å, the V2-V4 and V6-V6 distances grow from 2.95 Å to 3.06 Å and from 2.82 Å to 3.30 Å, respectively. As a consequence, two isolated V4-V6 vanadium pairs arise and the chain end atoms (V2) separate from the rest of the vanadium chain. In the 1-3-5 chain dimerization effects yield a shortened V5-V5 bond length both above and below the MIT. Obviously, in the insulating phase the V5-V5 pair separates even more from the

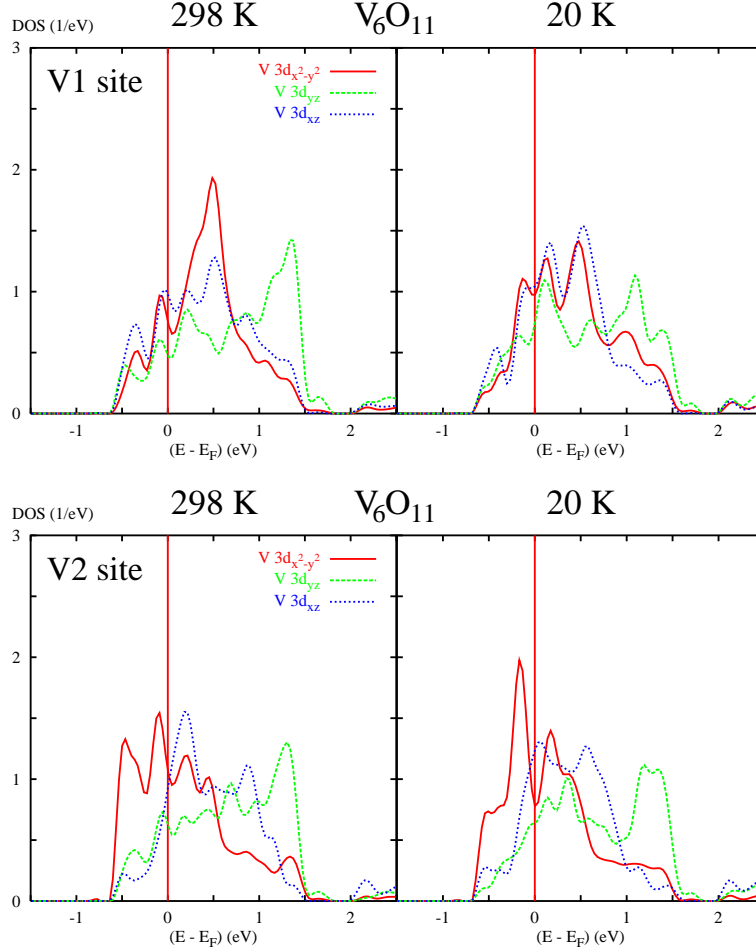


Fig. 11 Site-projected partial V $3d t_{2g}$ densities of states (DOS) per metal atom for the high and the low temperature crystal structure of V_6O_{11} : sites V1 and V2. The crystal structure is depicted in figure 9 and the orbitals refer to the local rotated reference frame.

evolving V1-V3 pairs. All these modifications of the crystal structure resemble the pairing effects known from the Peierls distortion in monoclinic VO_2 . Due to finite chains in the case of V_6O_{11} it is not surprising to find more complicated distortion patterns; the end atoms affect the V-V pairing in the whole chain.

The monoclinic phase of VO_2 is characterized not only by metal-metal pairing but also by zigzag-type in-plane displacements of the vanadium atoms along the local z -axis, thus along the diagonals of the rutile basal planes. While metal sites in the rutile structure coincide with the centers of the surrounding oxygen octahedra, they are shifted away from these positions by 0.20 \AA in the distorted configuration, thus giving rise to stronger V-O overlap. Equivalent shifts away from the centers of the octahedra are observed for the sites V3, V4, V5, and V6 in V_6O_{11} . The distance between vanadium atoms and octahedral centers grows from 0.16 \AA to 0.29 \AA (V3), from 0.17 \AA to 0.23 \AA (V4), from 0.07 \AA to 0.23 \AA (V5), and from 0.04 \AA to 0.35 \AA (V6), respectively. Actually, the major part of the shifts is oriented perpendicular to the c_{prut} -axis. Although the metal sites in the high temperature phase do not coincide with octahedral centers, the relative changes at the MIT are similar to VO_2 . Interestingly, the high temperature lateral displacements are larger for the intermediate sites V3 and V4 than for the center atoms V5 and V6. This is due to a slight rotation

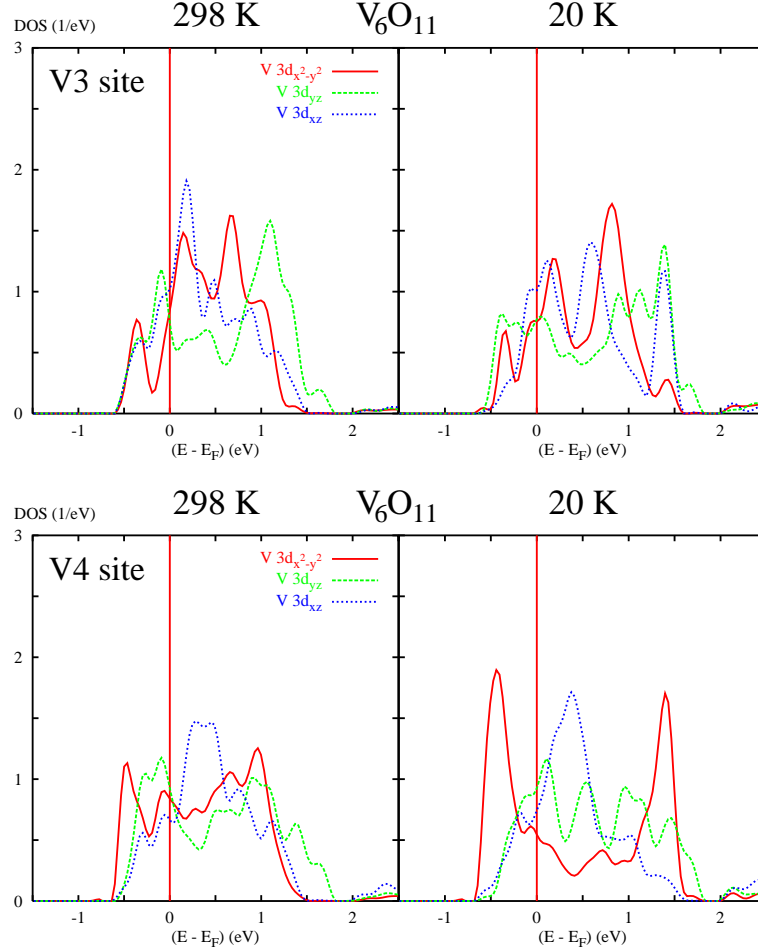


Fig. 12 Same representation as used in figure 11, but for the vanadium sites V3/V4.

of the vanadium chains away from the c_{prut} -axis, which is present in each Magnéli phase. Because of the rotation the chain end sites V1 and V2 shift away from their nearest neighbours along a_{prut} – resembling the vanadium anti-dimerization of V_2O_3 parallel to the c_{hex} -axis. Here the displacements of the metal sites with respect to octahedral centers amount to 0.18 Å (PM phase) and 0.21 Å (AFI phase). For V_6O_{11} these values are 0.32 Å in the metallic and 0.35 Å in the insulating phase. Hence, even concerning the details of the local distortion, chain centers and ends behave as their parent structures VO_2 and V_2O_3 .

Next we decompose the V $3d$ t_{2g} group of states into its symmetry components. Figures 11 to 13 give site-projected partial $d_{x^2-y^2}$, d_{yz} , and d_{xz} densities of states for the six inequivalent metal sites V1,...,V6. For each site the presentation of the data refers to the local rotated reference frame, which was defined in the discussion of the dioxide. The rutile reference frame is useful since the local octahedral coordinations of the metal sites in V_6O_{11} resemble the rutile arrangement, see the preceding sections.

We turn to the t_{2g} states of the vanadium atoms V4, V5, and V6, which are involved in strong dioxide-like displacements. Thus the site-projected densities of states are similar to one another and resemble the DOS of rutile and monoclinic VO_2 . Note the two peak structure weakly indicated in the high temperature V4 $d_{x^2-y^2}$ DOS due to σ -type V-V bonding along the metal chains. In the low temperature phase the V4-V6 dimerization causes an increased splitting of the DOS into bonding and antibonding branches located

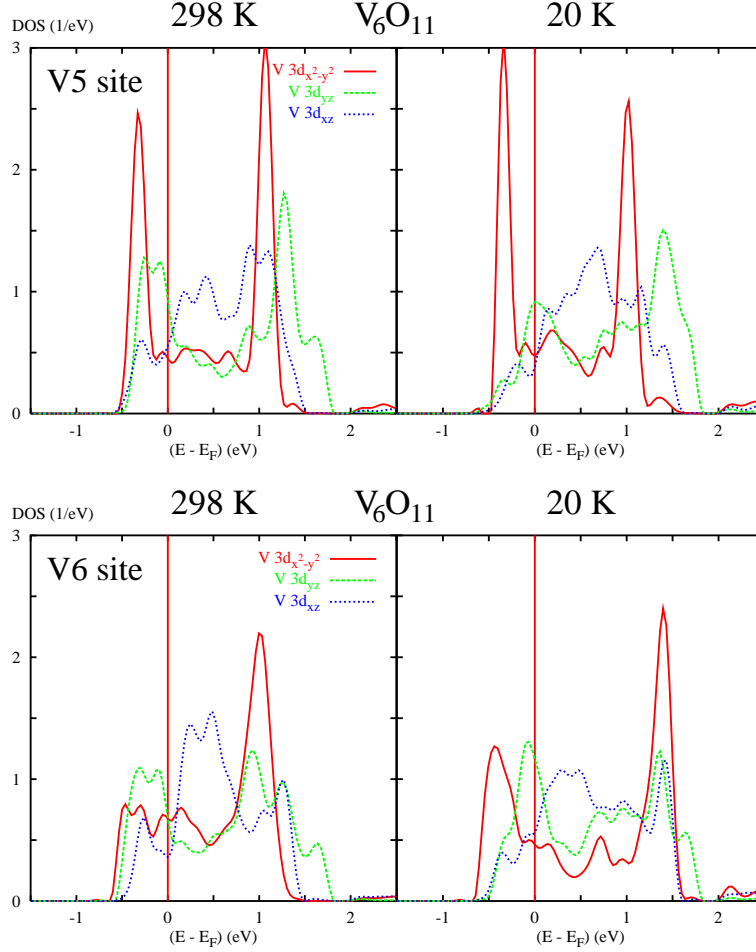


Fig. 13 Same representation as used in figure 11, but for the vanadium sites V5/V6.

at energies of -0.5 eV and 1.4 eV. The d_{yz} and d_{xz} densities of states undergo energetical upshifts due to the antiferroelectric displacements of the V4 atoms perpendicular to c_{prut} , which raise the overlap of V $3d$ and O $2p$ states and thus the π - π^* splitting. Similar to VO_2 , the energetical separation of the $d_{x^2-y^2} = d_{\parallel}$ band and the remaining e_g^{π} states is increased but not complete in the low temperature results.

The situation is similar for the V6 atoms, which participate in the V4-V6 pairs. Therefore the bonding and antibonding branches of the $d_{x^2-y^2}$ DOS appear at the same energies as for the V4 site. However, in the low temperature configuration the splitting is more pronounced due to additional V6-V6 bonding. As in the case of V4 the energetical upshift of the d_{yz}/d_{xz} DOS is easily observed, especially directly below the Fermi level. While the d_{xz} DOS of V4/V6 gives rise to a broad single peak, we find a distinct splitting of the d_{yz} DOS in contributions centered at about -0.2 eV and 1.0 eV for the high temperature structure. The splitting is understood by taking into account metal-metal bonding parallel to b_{prut} . Across octahedral faces typical sequences V2-V6-V4 appear in this direction, as obvious from figure 6. Due to a peak in the low temperature V6 d_{yz} DOS at about 1.4 eV, which is not present in the respective V4 DOS but reappears in the V2 DOS, we can assume increased V2-V6 bonding along b_{prut} at low temperatures. The $d_{x^2-y^2}$ and d_{yz} densities of states of atom V5 show strong bonding-antibonding splitting, which hardly changes at the transition. The shape of the $d_{x^2-y^2}$ DOS is understood in terms of constant V5-V5 bonding. In contrast,

splitting of the d_{yz} DOS traces back to V-V overlap along b_{prut} . The energetical upshift of these states at the MIT is pronounced and has the same origin as discussed for V4 and V6. In total, the partial V4, V5, and V6 densities of states display characteristic features known from the dimerization and the zigzag-type displacements in monoclinic VO_2 and are understood in terms of the latter compound.

In contrast to the chain center atoms V4, V5, and V6 the end atoms V1 and V2 are characterized by a sesquioxide-like local environment. Thus they are involved in V-V bonding across shared octahedral faces connecting the 1-3-5 to the 2-4-6 layers, but they are not subject to dimerization along c_{prut} . Hence, except for small peaks and shoulders around -0.5 eV and from 1.0 eV to 1.3 eV (reminiscent of the chain center $d_{x^2-y^2}$ densities of states) the V1/V2 $d_{x^2-y^2}$ DOS consists of a single broad peak extending from -0.2 eV to 0.7 eV. The subpeaks observed in this energy region miss counterparts in the DOS of any neighbouring vanadium atom. Since such peaks are indicative of metal-metal bonding we conclude, in consistence with the reported V-V distances, that chain end atoms are well separated from the remainder of the chains. Thus the $d_{x^2-y^2}$ states can be regarded as localized. While chain center $d_{x^2-y^2}$ orbitals predominantly mediate V-V overlap along c_{prut} , this interaction is suppressed for V1 and V2 for geometrical reasons. Hence the chain end $d_{x^2-y^2}$ states behave as the d_{xz} states, which generally give rise to reduced (π -type) metal-metal overlap along the chains. In both phases the center of weight of the V1 $d_{x^2-y^2}$ DOS is noticeably higher than that of the V2 $d_{x^2-y^2}$ DOS. Because of nearest neighbours along a_{prut} the d_{yz} orbitals are important for interpreting the chain end atoms since these states cause V-V bonding parallel to both a_{prut} and b_{prut} . The V1 and V2 d_{yz} states display bonding-antibonding splitting both above and below the transition. For the insulating modification this separation is more pronounced with peaks directly above the Fermi energy and around 1.2 eV. However, so far we are not able to distinguish between the effects of the different metal-metal interactions. Whether the shape of the d_{yz} DOS indicates bonding along a_{prut} or b_{prut} or both will be dealt with later. The question is of interest as the a_{prut} -direction of V_6O_{11} corresponds to the c_{hex} -axis of the corundum structure. Hence the splitting of the d_{yz} states is equivalent to the a_{1g} splitting in V_2O_3 and we can gain new insight into the MIT of the sesquioxide. The partial V1 and V2 t_{2g} densities of states resemble each other due to similar coordinations. They and are interpreted in accordance with V_2O_3 .

Atom V3 is exceptional as its t_{2g} DOS can neither be interpreted by means of dioxide-like dimerization in the vanadium chains nor by sesquioxide-like metal-metal overlap along a_{prut} . The second fact is simply due to the absence of adjacent vanadium sites, which allow for overlap between the 1-3-5 and 2-4-6 layers. Nevertheless, all components of the t_{2g} DOS are similar to those of sites V1 and V2. The $d_{x^2-y^2}$ and d_{xz} densities of states consist of broad single peaks. Reminiscent of bonding and antibonding branches in the corresponding V5 DOS we find satellite peaks at -0.4 eV and a shoulder at 1.0 eV in the high temperature phase. The compact shape of the d_{xz} DOS again is not surprising due to the small V-V overlap this orbital is involved in, not only for V3 but also for the other vanadium atoms. In contrast, the d_{yz} partial DOS reveals a distinct double peak structure in both phases, indicative of bonding-antibonding splitting. At first glance this finding is difficult to understand as geometrically no vanadium partner along a_{prut} exists, which could participate in V-V bonding. However, this puzzling situation is resolved by reconsidering the possibility of V-V interaction perpendicular to the chains and simultaneously perpendicular to the a_{1g} -direction, namely along b_{prut} . As mentioned before, there are finite vanadium sequences consisting of three atoms (V1-V5-V3), where the distance between neighbouring atoms corresponds to the longer rutile lattice constant. To be more precise, these bond lengths amount to $4.58 \text{ \AA}/4.54 \text{ \AA}$ (V1-V5) and $4.45 \text{ \AA}/4.40 \text{ \AA}$ (V5-V3) for the high/low temperature configuration. The associated values in the V2-V6-V4 sequences are $4.54 \text{ \AA}/4.57 \text{ \AA}$ (V2-V6) and $4.49 \text{ \AA}/4.38 \text{ \AA}$ (V6-V4). Since each vanadium atom in V_6O_{11} participates in σ -type overlap along b_{prut} , the bonding-antibonding splitting of the d_{yz} states is present not only for site V3.

This has important implications for the interpretation of the V1/V2 d_{yz} DOS because interactions parallel to a_{prut} and b_{prut} add to the bonding-antibonding splitting of these states. The respective antibonding peaks of V1 and V2 are merged at high temperatures but split up at the MIT. Due to the V-V overlap along b_{prut} site V3 resembles the electronic properties of the chain end sites, although its coordination does not allow for a_{1g} -like bonding. Therefore V-V bonding across the vanadium layers is not the only source for a splitting of the d_{yz} DOS. Despite differing bond lengths hardly any difference between V-V overlap via

octahedral faces within and perpendicular to the layers is found. Supporting results of Elfimov et al. [52], V-V couplings other than the a_{rut} -like are important for the shape of the a_{1g} bands in V_2O_3 .

While V-O overlap places the V $3d t_{2g}$ states near the Fermi level, the detailed electronic features of the orbitals, and thus the MIT of V_6O_{11} , are fundamentally influenced by the local metal-metal coordination. The small variations of the oxygen sublattice at the MIT barely affect the shape of any t_{2g} DOS, whereas modifications of the V-V bond lengths are important. Depending on the coordination, the local electronic properties of the vanadium atoms are typical for VO_2 or V_2O_3 and it is reasonable to regard the partial densities of states as local quantities. At the chain centers (V4, V5, V6) dimerization and antiferroelectric-like displacements via strong electron-lattice interaction cause a splitting of the $d_{x^2-y^2}$ DOS and an energetical upshift of the e_g^π states at the MIT. For atom V5 the former effect is already present at high temperatures. Summarizing, chain center atoms behave analogous with VO_2 . In contrast, at the chain ends (V1, V2, V3) the $d_{x^2-y^2}$ orbitals are characterized by strongly reduced metal-metal overlap and show a localized nature. The shape of the $d_{x^2-y^2}$ DOS is closely related to the d_{xz} DOS. Due to the strong localization, electronic correlations are important for the chain end $d_{x^2-y^2}$ states. Being subject only to in-layer V-V overlap, the partial V3 d_{yz} DOS shows bonding-antibonding splitting similar to the atoms V1 and V2, which have an additional nearest neighbour across the layers. Therefore the in-plane V-V interaction is at least as important as the perpendicular overlap. In conclusion, the sesquioxide-like regions of the V_6O_{11} crystal appear to be susceptible to electronic correlations for geometrical reasons. Structural variations at the MIT leave all three components of the t_{2g} partial DOS almost unchanged, thus reflecting close relations to V_2O_3 . We interpret the phase transition of V_6O_{11} as resulting from a combination of electron-lattice interaction and electronic correlations. Due to the different atomic arrangements in VO_2 and V_2O_3 -like regions neither an embedded Peierls instability nor correlations can account for the MIT of V_6O_{11} on their own.

Going back to the calculated valence charges at the vanadium and oxygen sites summarized in table 3 we investigate possible charge ordering. Different atomic spheres radii, necessary to fulfill the requirements of the atomic sphere approximation, prohibit a quantitative comparison of the valence charges but allow still for qualitative results. For the high temperature modification there are about 0.2 electrons less at sites V1 and V3 than at sites V2 and V4, whereas the charges at the central sites V5 and V6 coincide. The atomic spheres comprise almost the same space for the pairs V1/V2, V3/V4, and V5/V6, respectively. In general, the calculated 2.5/2.7 V $3d$ valence electrons contradict the simple ionic picture predicting an average of 1.33 electrons per vanadium atom. Instead of $V^{3.67+}$ ions we find $V^{2.3+}$ and $V^{2.5+}$ configurations, which is not surprising due to covalent V-O bonding. Oxygen spheres comprise about four $2p$ electrons. Further electrons enter the empty spheres and hence the open space between vanadium and oxygen.

The accuracy of comparing calculated valences is limited as the assignment of charge to specific sites is arbitrary to some degree. We assign charge within an atomic sphere to the respective atomic site. Electrons entering interstitial empty spheres cannot be assigned to any specific atom. Importantly, differences in the occupation of equivalent states can be identified with a much higher accuracy. Thus the $3d$ charge of both V1 and V3 is significantly reduced. In addition, we obtain the same result for the low temperature phase, where all vanadium spheres show similar radii. The valence charge at sites V1, V3, and V5 is roughly 0.2 electrons smaller than at sites V2, V4, and V6, resulting in a charge transfer of 0.1 electrons per site from the 1-3-5 to the 2-4-6 chain above and below the MIT. The different electron count in the two metal chains is related to their crystallographic inequivalence. While donor atoms (to some extent) approach the VO_2 charge configuration, the acceptor chain resembles more the V_2O_3 filling. The electronic configurations of VO_2 and V_2O_3 seem preferable to a mixture of both. However, chain end sites do not generally gain excess charge at the expense of the dioxide-like chain centers. Hence it is not the electron count of a specific atom but the local coordination which determines the behaviour at the phase transition. The calculated valence charges contradict V^{3+}/V^{4+} states, but confirm two kinds of metal valences; they point to smaller charge differences. Deviations from the ionic picture are consistent with susceptibility data by Gossard et al. [13], whereas for the insulating phase we do not find the proposed charge ordering.

The above findings have important implications for understanding V_2O_3 as the chain end atoms of the Magnéli phases resemble the local metal coordination of this material. According to the previous discussion the electronic properties of V_6O_{11} are influenced by essentially three effects. First, the center atoms of the vanadium chains along c_{prut} reflect characteristics of the embedded Peierls instability responsible for the MIT in VO_2 . Second, the localization of the chain end $d_{x^2-y^2}$ orbitals leaves them susceptible to electronic correlations. Third, the chain end d_{yz} orbitals to roughly equal parts are subject to both metal-metal bonding within (along b_{prut}) and perpendicular to (along a_{prut}) the vanadium layers. As vanadium chains in the case of V_2O_3 ($n = 2$) degenerate to pairs, a dioxide-like Peierls instability cannot contribute as a matter of principle. However, the localized nature of the $d_{x^2-y^2}$ orbitals and the importance of strong V-V coupling along b_{prut} should be transferred to the sesquioxide. Due to the high crystal symmetry both effects could not be analyzed in previous studies of V_2O_3 . As a consequence of the broken symmetry in the Magnéli phases, combined with a closely related coordination of appropriate vanadium atoms, they are accessible to the study of V_6O_{11} . The splitting of the a_{1g} -like states due to metal-metal overlap along c_{hex} therefore seems to be less important than commonly assumed for V_2O_3 .

6 Band narrowing in V_4O_7

The compound V_4O_7 is suitable for studying chain end effects since the metal chains here comprise only four atoms [73]. Analogous with the preceding section we discuss the electronic structure and its changes at the MIT in relation to the simultaneous structural transformations. Applying the knowledge established in the study of V_6O_{11} we can group the electronic bands into states behaving either VO_2 or V_2O_3 -like.

Partial V $3d$ and O $2p$ densities of states arising from the high and low temperature structure are shown in figure 14. As for VO_2 , V_2O_3 , and V_6O_{11} , we find three separated groups of electronic bands. Recalling the molecular orbital picture, the bonding-antibonding splitting due to V-O overlap, and the discussions in the previous sections, we identify the bonding states with those bands extending from -8.3 eV to -3.3 eV at high temperatures; they shift to the region from -8.2 eV to -3.0 eV below the MIT. Further groups of bands correspond to π^* and σ^* states. Hence they are dominated by vanadium states and separate into t_{2g} and e_g^σ contributions due to the octahedral coordination of the metal sites. While the t_{2g} group is observed between -0.7 eV and 1.6 eV in the metallic phase, its upper edge shifts to 1.7 eV at low temperatures. The e_g^σ group starts at 2.0 eV in both phases, but it extends to 4.7 eV instead of 4.4 eV in the insulating phase. Since the unit cell of V_4O_7 contains 8 vanadium and 14 oxygen atoms we have $8 \times 2 = 16$ vanadium $3d$ e_g^σ , $8 \times 3 = 24$ vanadium $3d$ t_{2g} , and $14 \times 3 = 42$ oxygen $2p$ bands. Hybridization between V $3d$ and O $2p$ orbitals results in finite contributions of vanadium in the bonding and of oxygen in the antibonding region. As expected, such hybridization effects are stronger for σ -type V-O overlap. Moreover, there is a finite t_{2g} DOS in the e_g^σ dominated region. As the magnitude of this admixture equals the result for V_6O_{11} , deviations from an ideal octahedral coordination of the vanadium sites are similar in both compounds and likewise similar to the sesquioxide. All these results for V_4O_7 fit very well into the picture developed in the preceding sections. Due to the formal V $3d$ charge of 1.5 electrons per metal site, V_4O_7 systematically is between V_6O_{11} and V_2O_3 . Therefore the V $3d$ t_{2g} orbitals are filled to a somewhat larger extent than for V_6O_{11} , which is confirmed by figures 10 and 14. Although the calculation misses an energy gap for the experimental insulating phase, the LDA shortcomings again do not affect an investigation of relations between structural and electronic properties or the analysis of implications for the MIT.

While the previous analysis of V_6O_{11} gave strong indications for a predominant influence of electron-lattice interaction in dioxide-like and of electronic correlations in sesquioxide-like regions of the crystal, we expect that the investigation of the sesquioxide-related member V_4O_7 will allow for conclusions about the MIT of V_2O_3 . Separated by oxygen atoms, inequivalent vanadium layers alternate along the a_{prut} -axis of V_4O_7 , comprising the atoms V1/V3 or V2/V4. Due to this alternation and due to relative shifts of the metal 4-chains along c_{prut} the end sites V1 and V2 are located on top of each other, see figure 8. We again refer the V $3d$ orbitals to local coordinate systems with the z -axis oriented parallel to the apical axis of the

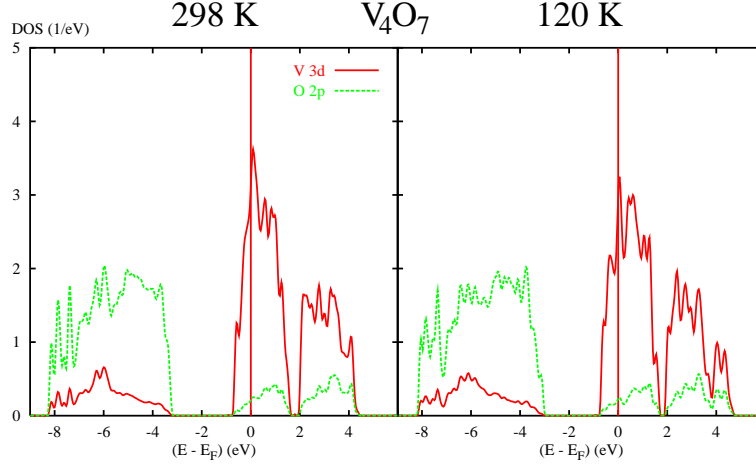


Fig. 14 Partial V 3d and O 2p densities of states (DOS) per vanadium atom resulting from the high (298 K) and low (120 K) temperature structure of the compound V_4O_7 .

local octahedron and the x -axis parallel to c_{prut} , respectively. Using this reference frame, a decomposition of the V 3d t_{2g} group of states into the symmetry components $d_{x^2-y^2}$, d_{yz} , and d_{xz} is depicted in figures 15 and 16. The site-projected partial densities of states are given for the vanadium sites V1, V2, V3, and V4. In the following, we concentrate on the results for the 1-3 chain, which is motivated by the fact that the modifications of the local surroundings of atom V1 at the MIT are similar to those known from V_2O_3 . According to the data denoted in figure 8 the V1-V2 and V1-V3 distances increase at the MIT, as do the distances a and b in the sesquioxide at the PM-AFI transition, see figure 4. Since in the latter compound all vanadium atoms are crystallographically equivalent a complete symmetry analysis of the electronic states cannot be performed. However, this is possible for V_4O_7 . As demonstrated in the case of V_6O_{11} , the local atomic arrangements are related to the electronic structures of the respective sites. Therefore the V1 site of V_4O_7 allows us to study the influence of the structural changes at the MIT of V_2O_3 in more detail than in a direct investigation.

Changes in the V_4O_7 crystal structure at 250 K are mainly concerned with strong dimerization evolving in both the 1-3 and 2-4 metal chain, see figure 8. While the V3-V3 and V2-V4 bond lengths shorten from 2.79 Å and 2.93 Å to 2.67 Å and 2.83 Å, the remaining distances V1-V3 and V4-V4 elongate from 2.97 Å and 2.93 Å to 3.03 Å, respectively. Hence we find an isolated V3-V3 pair in the first and two V2-V4 pairs in the second chain. In the 1-3 chain the end atoms decouple to a large degree from the central V3-V3 pair. The modifications resemble pairing effects associated with the embedded Peierls instability of the dioxide. Nevertheless, the end atoms of the 1-3 chain likewise show structural changes known from the symmetry breaking PM-AFI transition of V_2O_3 . The distance between V1 and the nearest vanadium site along c_{prut} increases by 0.06 Å, which is half the shift found for the sesquioxide. Note that the dominating structural changes in V_2O_3 do not appear along a_{prut} but along c_{prut} . In contrast to the 1-3 chain, the end atoms of the 2-4 chain increase the coupling to adjacent in-chain sites below the MIT. Thus they show the opposite trend than found in V_2O_3 and are not suitable for investigating the latter material.

Beyond metal-metal pairing also zigzag-type in-plane displacements of the metal sites are present in the V_4O_7 structure. The distances between vanadium atoms and octahedral centers amount to 0.31 Å/0.35 Å (V1), 0.32 Å/0.27 Å (V2), 0.15 Å/0.17 Å (V3), and 0.08 Å/0.09 Å (V4) in the high/low temperature modification. Apparently, the average bond length does not increase at the transition, which contrasts findings for VO_2 and V_6O_{11} , hence confirming the sesquioxide-like character of V_4O_7 . Because of a slight rotation of the vanadium chains away from the c_{prut} -axis, the lateral displacement is much larger for the chain end

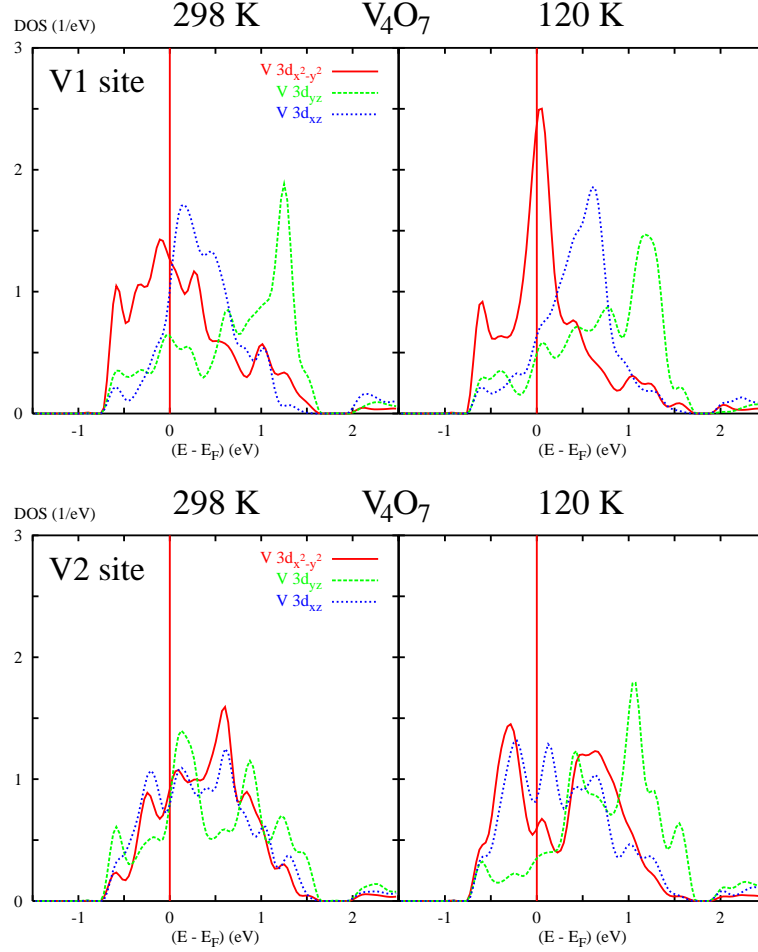


Fig. 15 Site-projected partial V $3d t_{2g}$ densities of states (DOS) per metal atom for the high and the low temperature crystal structure of V_4O_7 : sites V1 and V2. The crystal structure is depicted in figure 8 and the orbitals refer to the local rotated reference frame.

sites V1 and V2. The rotation enables the latter sites to increase their distance along a_{prut} , which reflects the anti-dimerization of V_2O_3 parallel to c_{hex} . In general, the main part of the zigzag-type displacements is oriented perpendicular to c_{prut} . Atom V2 shifts almost along the apical axis of its octahedron, i.e. along the local z -axis, whereas atom V1 moves perpendicular to the local z -axis. However, because of the rotation of the local coordinate system by 90° around the c_{prut} -axis, the displacements occur in every chain along the same direction. On closer inspection we recognize the motions to be antiparallel, which increases the in-pair V1-V2 bond length. Altogether, the zigzag-type antiferroelectric mode of the 2-4 chain resembles the behaviour of the dioxide, whereas the 1-3 chain reveals distinct differences above as well as below the MIT. In retrospect, this interrelation applies also to V_6O_{11} because the displacements of the dioxide-like 1-3-5 chain point along the local z -axis rather than those of the 2-4-6 chain.

Decomposing the V $3d t_{2g}$ partial DOS, we observe in figures 15 and 16 for the $d_{x^2-y^2}$ states a similar behaviour as in VO_2 . Due to strong σ -type V-V bonding along the vanadium chains the chain center sites show distinct splitting of the $d_{x^2-y^2}$ DOS. In the case of atom V3 a broad peak is observed from roughly -0.7 eV to 0.3 eV and a sharp peak at 1.0 eV. Because of weaker V4-V4 bonding the splitting is smaller

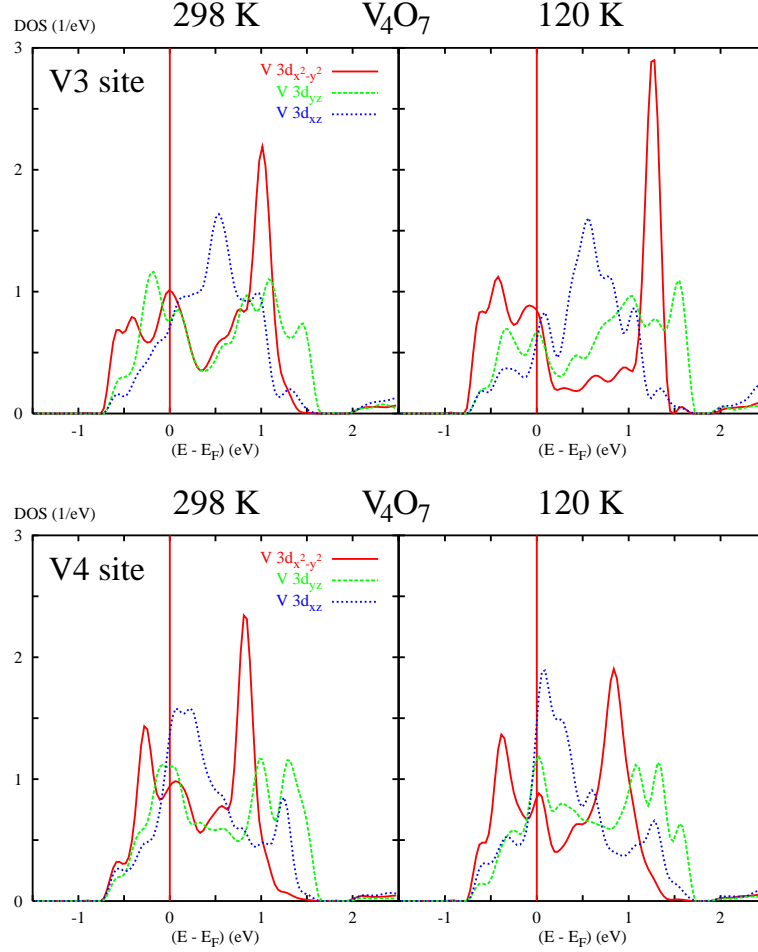


Fig. 16 Same representation as used in figure 15, but for the vanadium sites V3/V4.

for the V4 site with peaks at approximately -0.3 eV and 0.8 eV. The chain end atoms V1 and V2 are less affected by in-chain metal-metal bonding and consequently display a more compact $d_{x^2-y^2}$ DOS. At low temperatures the behaviour of both metal chains changes substantially. Increased V-V dimerization yields enhanced bonding-antibonding splitting of the V3 $d_{x^2-y^2}$ DOS. Additionally, by virtue of reduced V1-V3 overlap along c_{prut} the V1 $d_{x^2-y^2}$ states tend to localize. Accordingly, the V1 $d_{x^2-y^2}$ DOS sharpens and develops a pronounced peak near the Fermi energy at low temperatures. While the V4-V4 distance grows by 0.1 Å below the transition, the coupling of the V4 atoms to the chain end sites increases. The reduced V2-V4 bond length causes stronger bonding-antibonding splitting of the V2 $d_{x^2-y^2}$ DOS.

Modifications of the vanadium d_{xz} partial DOS at the transition are less significant. They consist mainly of an energetical up and downshift of the states as observed for atoms V1 and V2, respectively. Such shifts are due to increased and decreased displacements perpendicular to c_{prut} . Moving vanadium atoms laterally off the centers of gravity of their oxygen octahedra modifies the overlap between V $3d$ and O $2p$ orbitals. The oxygen sublattice itself is hardly affected by the structural transformations. Therefore the shifts of the d_{xz} states can be understood in terms of a zigzag-type antiferroelectric distortion of the vanadium chains. As the distortion is reduced for the chain center sites V3 and V4, see the former discussion, the effects are barely visible in the DOS. In the prototypical case of VO_2 lateral displacements are found only in the low

temperature monoclinic phase, whereas V_4O_7 reveals them similar at all temperatures. Since metal-metal bonding is less important for d_{xz} orbitals no bonding-antibonding splitting is visible.

The situation is more complicated for d_{yz} orbitals, which are considerably influenced by different kinds of hybridization. Recall from our earlier investigations that these electrons can be involved in metal-metal overlap across octahedral faces both along a_{prut} and b_{prut} . Moreover, antiferroelectric-like displacements of the vanadium atoms lead to increased overlap between V 3d and O 2p states, which causes energetical upshift of the antibonding vanadium dominated states. In the case of V_4O_7 the atoms V3 and V4 display neither relevant antiferroelectric shifts nor V-V interaction parallel to the a_{prut} -axis. There are simply no nearest metal neighbours in this direction. As a consequence, the pronounced double peak structure of the V3/V4 d_{yz} DOS indicates bonding-antibonding splitting due to V1-V3 and V2-V4 overlap, respectively, which is true at high and low temperatures. Analogous with the finite metal 3-chains of V_6O_{11} along b_{prut} we are confronted with vanadium pairs giving rise to V1-V3 and V2-V4 bonding across shared octahedral faces. In contrast to the central vanadium atoms the chain end atoms V1 and V2, apart from participating in V1-V3/V2-V4 overlap along b_{prut} , take part in V1-V2 bonding along a_{prut} . The partial V1 and V2 d_{yz} densities of states thus consist of features reminiscent of the sites V2/V3 and V1/V4, respectively. Being subject to two different types of metal-metal overlap, the d_{yz} orbitals of the chain end atoms undergo two intertwining bonding-antibonding splittings, which lead to complicated triangular DOS shapes, especially in the low temperature phase, and resemble the shape of the V 3d a_{1g} DOS of V_2O_3 . In addition, the form is affected by the discussed zigzag-type displacements of the chain end atoms, which intensify the metal-oxygen bonding. As a consequence, the center of gravity of the V1/V2 d_{yz} DOS shifts to higher energies below the MIT. Changes in the shape of the V2 d_{yz} DOS yield a closer resemblance to the V1 d_{yz} DOS, which can be traced back to an improved coupling between the chain end atoms at low temperatures. As the relative displacements of the sites V1 and V2 along c_{prut} are reduced, the V1-V2 bond penetrates the octahedral faces along a_{prut} more favorably and the overlap becomes more effective.

In conclusion, the electronic structure of V_4O_7 is strongly influenced by the coordination of the metal sites, as previously reported for V_6O_{11} . Generally, while the overlap of V 3d and O 2p orbitals places the V 3d t_{2g} states close to the Fermi energy, the details of the electronic structure are subject to metal-metal bonding. In particular, one finds a distinct bonding-antibonding splitting of the $d_{x^2-y^2}$ states at the chain center sites. In the low temperature phase the same applies to atom V2. All these splittings are analogous with the corresponding orbitals in VO_2 and V_6O_{11} , where they likewise are enforced by V-V dimerization. In contrast, the V1 $d_{x^2-y^2}$ DOS reveals a compact structure and a distinct sharpening below the MIT as these states hardly take part in the dimerization along the metal chains. Hence they may be susceptible to electronic correlations. For the d_{xz} and d_{yz} states we find noticeable response to the displacements of the metal atoms perpendicular to c_{prut} . As the atoms move relative to the octahedral centers, states with d_{xz} and d_{yz} symmetry display energetical up and downshifts in the vanadium and oxygen dominated regions, respectively. However, the d_{yz} DOS is affected mainly by the V-V bonding across shared octahedral faces. Chain center sites are subject to bonding only along b_{prut} and show a characteristic two peak structure. In contrast, atoms V1 and V2 additionally take part in d_{yz} -type overlap along a_{prut} , leading to densities of states similar to the a_{1g} DOS of V_2O_3 . The latter orbital mediates V-V bonding along $c_{\text{hex}} = a_{\text{prut}}$.

Similar to the V_6O_{11} findings, the LDA results indicate small charge transfer between the two inequivalent metal chains. Recall the limitations of assigning charge to specific atomic sites as discussed in section 5. According to table 5 the V2 sites comprise 0.2 electrons less than the V1 sites in the high temperature modification of V_4O_7 , while V3 and V4 show similar values. Note that in the pairs V1/V2 and V3/V4 the sphere radii are almost equal. The interpretation of the low temperature results is a little more complicated. However, taking into account the various sphere radii one can state reduced charges for both V2 and V4, where the charge deficit is 0.2 electrons per site. Of course, the calculated values of 2.6-2.8 V 3d valence electrons do not agree with the ionic picture predicting 1.5 electrons per metal atom – but due to covalent V-O bonding this deviation is not surprising. In comparison to V_6O_{11} the atomic spheres of V_4O_7 comprise slightly more charge, which reflects the position of the compound in the Magnéli series. We find no significant differences in the charges of the particular oxygen spheres since each of them contains about

four $2p$ electrons. Further electrons enter the interstitial empty spheres and thus are difficult to classify in vanadium and oxygen-type contributions. Altogether we observe a charge transfer of about 0.1 electrons per site from the 2-4 to the 1-3 chain. In the high temperature phase only the chain end sites are involved in the transfer. As in the case of V_6O_{11} the different electron count is related to the crystallographical inequivalence of the two vanadium chains. While the 2-4 donor chain becomes slightly more VO_2 -like, the 1-3 acceptor chain to some extent approaches the V_2O_3 configuration. These LDA findings qualitatively confirm x-ray results by Marezio et al. [10], who applied an ionic picture and reported chains of V^{3+} and V^{4+} ions running parallel to the c_{prut} -axis. Although an ordered arrangement of varying valence charges is confirmed by the calculation, the charge discrepancy is much smaller due to covalent bonding. Nuclear magnetic resonance findings by Gossard et al. [9] support chains of differently charged atoms along c_{prut} but indicate incomplete differentiation into 3+ and 4+ valences. The authors observed a slightly increased charge ordering below the MIT, which is confirmed by the LDA results.

As in other Magnéli phases, particularly in V_6O_{11} , the electronic structure of V_4O_7 is a mixture of features characteristic of either vanadium dioxide or sesquioxide. The local atomic environment of the chain end site V1 bears close resemblance to the V_2O_3 structure as it is subject to an increased separation from its vanadium neighbours at the MIT. We are thus in a position to transfer some of the above conclusions for V_4O_7 to V_2O_3 . First, V-V bonding across octahedral faces along a_{prut} seems to have the major effect on the shape of the d_{yz} DOS of V_4O_7 and thus on the shape of the a_{1g} DOS of V_2O_3 . However, also the V-V hybridization across the faces parallel to b_{prut} is large since it leads to strong splitting of the electronic states. Second, due to the reduced metal-metal interaction across the octahedral edges parallel to c_{prut} the vanadium $d_{x^2-y^2}$ states are substantially localized and undergo further localization at the transition.

This supports previous work by Dernier [41], who concluded from a comparison of pure/doped V_2O_3 and of Cr_2O_3 that the metallic properties of V_2O_3 are connected to V-V hybridization across shared octahedral edges rather than to hopping processes in the vanadium pairs along c_{hex} . From this point of view the MIT arises from structural changes occurring at the transition. Via strong electron-phonon coupling the structural distortions translate into a narrowing of the bands perpendicular to the c_{hex} -axis. Note that the decoupling of the vanadium atoms parallel to the c_{prut} -direction is even stronger for the sesquioxide than for V_4O_7 since the corresponding bond length shortens by 0.12 Å instead of 0.06 Å. The band narrowing eventually paves the way for increased influence of electronic correlations in the insulating configuration. So far our treatment of V_2O_3 concerned only the symmetry breaking PM-AFI transition, which is accompanied by substantial modifications of the interatomic V-V spacings. However, Pfalzer et al. [42] reported on local symmetry breaking in the PI phase of aluminium doped V_2O_3 , giving rise to similar structural and electronic properties of the AFI and PI phase at least on a local scale. Due to the local distortions one may expect a closely related scenario for both the PM-AFI and the PM-PI transition. In general, the reduction of the dispersion perpendicular to c_{hex} seems to play a key role for the MIT of V_2O_3 .

7 Systematic aspects of the Magnéli series

Finally, addressing the systematics inherent in the Magnéli series we are interested in effects of the chain length. Variation of the length systematically modifies the ratio of dioxide and sesquioxide-like regions. In this context especially a comparison of V_7O_{13} and V_8O_{15} is useful because the materials are structurally very similar. Nevertheless, the former compound is the only member of the Magnéli series which does not undergo an MIT as a function of temperature. In a comparison of all Magnéli phases, VO_2 and V_2O_3 take an exceptional position as they either miss chain end or chain center metal sites. In addition, they display higher symmetry than that of the triclinic space group $P\bar{1}$ (C_i^1). This is likewise true for monoclinic V_3O_5 . The latter compound, although even closer related to the sesquioxide than V_4O_7 , is therefore not suitable for a detailed understanding of the electronic states in V_2O_3 . Both V_5O_9 and V_8O_{15} are characterized by a superstructure doubling the unit cell at the MIT. While the metal chains of low temperature V_5O_9 [74, 75] lose their inversion symmetry, there are four inequivalent chains for V_8O_{15} . The notation of the vanadium

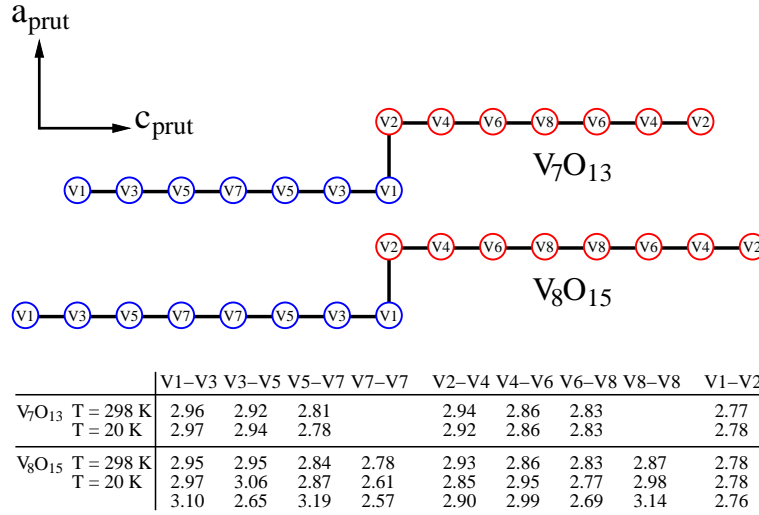


Fig. 17 Notation of the vanadium sites in V_7O_{13} and V_8O_{15} , where we observe metal chains of length $n = 7/n = 8$ along c_{prut} . In both cases eight inequivalent vanadium sites give rise to two types of chains. The spacial arrangement of the chains is similar to that of V_4O_7 and V_6O_{11} , see figures 8 and 9. The table gives measured V-V distances (in Å) for both the metallic (298 K) and the insulating (20 K) phase of V_7O_{13}/V_8O_{15} [60]. Below the transition the latter compound develops a superstructure with four inequivalent chains.

sites in V_7O_{13}/V_8O_{15} is given in figure 17. For the former compound the chains are labeled V1-V3-V5-V7-V5-V3-V1 and V2-V4-V6-V8-V6-V4-V2, whereas for V_8O_{15} the innermost site is doubled, leading to the configurations V1-V3-V5-V7-V7-V5-V3-V1 and V2-V4-V6-V8-V8-V6-V4-V2. Extra sites in the insulating superstructure are indicated by tildes. As in V_4O_7 and V_6O_{11} , the oxygen sublattice of V_8O_{15} hardly changes at the phase transition. The dominating structural modifications are again concerned with the V-V dimerization along c_{prut} , see the bond lengths in figure 17.

The study of V_7O_{13}/V_8O_{15} is again based on LDA calculations, which were performed analogous with the previously discussed Magnéli phases. The partial DOS shows three groups of bands corresponding to O 2p, V 3d t_{2g} , and V 3d e_g^σ states. Due to a reduced formal electron count of 1.29 and 1.25 electrons per metal site for the $n = 7$ and $n = 8$ compound, respectively, the filling of the t_{2g} group is slightly smaller than for V_4O_7 and V_6O_{11} . Site-projected partial densities of states for V_7O_{13} and V_8O_{15} show the typical features discovered before. In particular, the shape of the DOS curves is completely understood in terms of the vanadium coordination, which is true for all Magnéli compounds. Hence it is useful to concentrate on representative atomic sites: the central site V7 and the last but one site V3 of the 1-3-5-7 chain.

Figure 18 shows site-projected partial densities of states for the sites V3 and V7 arising from the room temperature structures of V_7O_{13} and V_8O_{15} . The representation of the V 3d symmetry components refers to the local rotated reference frame with the z and x -axis parallel to the apical axis of the local octahedron and the c_{prut} -axis, respectively. V-O overlap combined with crystal field splitting results in two groups of antibonding states. While the t_{2g} dominated region reaches from about -0.6 eV to 1.8 eV, one observes additional t_{2g} contributions above 2.0 eV, where the e_g^σ states dominate. In consistence with the positions of V_7O_{13} and V_8O_{15} within the Magnéli series, the latter are fairly small, which resembles the behaviour of VO_2 rather than of V_2O_3 . Contributions due to O 2p orbitals in the energy interval of figure 18, which arise from covalent V-O bonding, comprise less than 10% of the total DOS at the Fermi level; they are not included in the figure. As a matter of fact, the in-chain V-V distances in the high temperature modifications of V_7O_{13} and V_8O_{15} are very similar, see figure 17. Of course, additional V7-V7 and V8-V8 bonds occur for chains of length $n = 8$, which are not available for chains of length $n = 7$. The oxygen sublattice of the

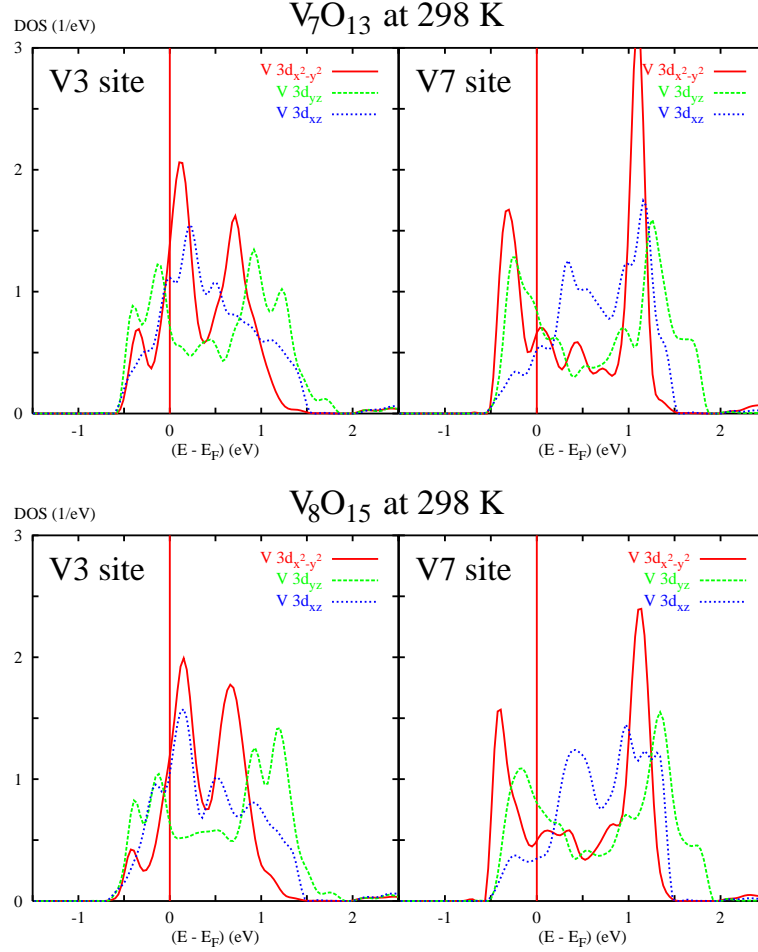


Fig. 18 Site-projected partial V $3d\ t_{2g}$ densities of states (DOS) per vanadium atom for high temperature V_7O_{13} and V_8O_{15} . The orbitals refer to the local rotated reference frame. Sites V3 and V7 reveal little discrepancy.

compounds is almost identical, which likewise applies to the antiferroelectric-like lateral displacements of the metal atoms perpendicular to c_{prut} and the rotation of the metal chains off the c_{prut} -axis. Compared to V_4O_7 and V_6O_{11} the latter effects are weaker due to the dioxide-like nature of the long chain compounds. The importance of the local atomic coordination for the DOS shape suggests a similar electronic structure for both metallic V_7O_{13} and V_8O_{15} , which is confirmed by figure 18.

The local $d_{x^2-y^2}$, d_{yz} , and d_{xz} densities of states resemble one another even with regard to the details of their shapes, which applies not only to the sites V3 and V7 but also to all other metal atoms. Due to strong σ -type metal-metal bonding along c_{prut} the chain center atoms are characterized by a distinct splitting of the $d_{x^2-y^2}$ DOS. In the case of V7 we hence find sharp peaks at about -0.3 eV and 1.1 eV. Because of the increasing V-V distances at the chain ends the bonding-antibonding splitting is noticeably smaller for the V3 $d_{x^2-y^2}$ DOS, where peaks occur at about 0.2 eV and 0.7 eV. As a consequence of less efficient π -type V-V overlap via the d_{xz} orbitals the respective DOS is rather compact. In contrast, a substantial splitting in bonding and antibonding branches can be found in the d_{yz} DOS. For sites V3 and V7 this shape traces back to metal-metal interaction along b_{prut} . The strength of the splitting is roughly identical for both sites. To conclude, the site-projected densities of states of high temperature V_7O_{13}/V_8O_{15} are well understood

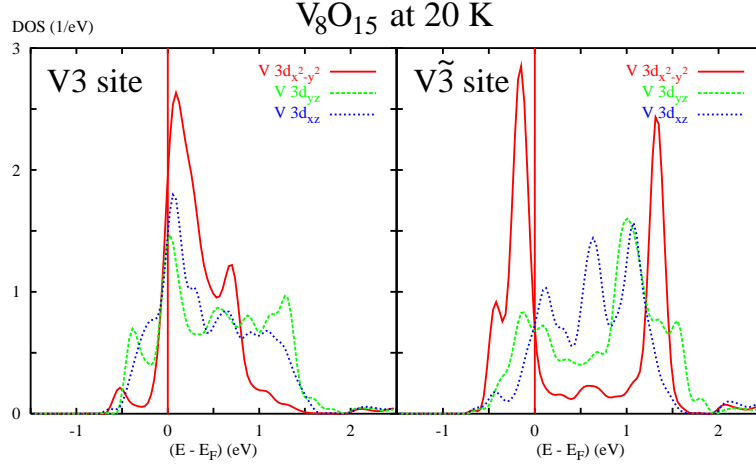


Fig. 19 Site-projected partial V $3d t_{2g}$ densities of states (DOS) per metal atom for sites V3 and $\tilde{V}3$ of low temperature V_8O_{15} . At high temperatures these sites are equivalent. The orbitals refer to the local rotated reference frame.

from the discussions in the preceding sections. By virtue of very closely related metal-metal bond lengths in the compounds similar DOS curves arise. Thus it is surprising that only one of the materials undergoes an MIT. While the charges in the 1-3-5-7 chain of V_7O_{13} and the 2-4-6-8 chain of V_8O_{15} are more or less equally distributed among the metal sites, the other chains show a small shift of charge towards the chain centers, but generally such charge transfer effects are very small. In the calculation the metallic phases of V_7O_{13} and V_8O_{15} are barely distinguishable as far as the local electronic behaviour is concerned.

The investigation of the low temperature V_8O_{15} modification reveals the same mechanisms found previously in the Magnéli series. Depending on the bond lengths to the adjacent vanadium sites along c_{prut} one finds either increased splitting or enhanced localization of the $d_{x^2-y^2}$ orbitals. The V-V bond lengths indicate strong V-V dimerization in the $\tilde{1}-\tilde{3}-\tilde{5}-\tilde{7}$, 2-4-6-8, and $\tilde{2}-\tilde{4}-\tilde{6}-\tilde{8}$ chain, but not in the 1-3-5-7 chain. While the innermost V-V distances of both the 2-4-6-8 and $\tilde{2}-\tilde{4}-\tilde{6}-\tilde{8}$ chain elongate at the MIT from 2.87 Å to 2.98 Å and 3.14 Å, they shorten for the other chains from 2.78 Å to 2.61 Å and 2.57 Å. Thus the dimerization patterns are inversed. As a consequence, in the low temperature structure all vanadium sites, except for V1, V3, V5, and $\tilde{V}1$, are involved in strong V-V overlap along c_{prut} . The increased interaction leads to a stronger bonding-antibonding splitting of the $d_{x^2-y^2}$ DOS. For atoms affected by V-V dimerization one additionally obtains energetical upshifts of the d_{yz} and d_{xz} densities of states. In accordance with earlier findings they show typical changes in the electronic structure known from the MIT of VO_2 . Although the energetical separation between the $d_{x^2-y^2}$ states and the remaining e_g^π states of V_8O_{15} grows in the low temperature phase it is still far from complete. The described Peierls-like behaviour does not account for sites V1, V3, V5, and $\tilde{V}1$, which are characterized by decreasing V-V overlap below the MIT. Due to the reduced metal-metal bonding the $d_{x^2-y^2}$ densities of states sharpen and develop a pronounced peak close to the Fermi level. Because of their sesquioxide-like coordination the behaviour is not surprising for sites V1 and $\tilde{V}1$. However, the separation from neighbouring vanadium atoms forces V3 and V5 to display the same localization of the $d_{x^2-y^2}$ orbitals. Hence electronic correlations may be as important for these states as for the V_2O_3 -type chain end sites. The question why one of the four vanadium chains in the low temperature V_8O_{15} superstructure prefers localization to dimerization is difficult to answer. The calculated V $3d$ valence charges do not give rise to any systematics. Partial t_{2g} densities of states are depicted in figure 19. For the dioxide-like $\tilde{V}3$ site we recognize both an increased splitting of the $d_{x^2-y^2}$ DOS and an energetical upshift of the d_{yz} and d_{xz} curves. In contrast, the structurally separated V3 site is characterized by a very

compact $d_{x^2-y^2}$ DOS located almost completely above the Fermi level. In comparison to the sesquioxide-like V1 site of V_4O_7 , see figure 15, the filling of the low temperature $d_{x^2-y^2}$ states is significantly smaller due to the reduced electron count. Summarizing, these findings support our MIT scenario as a mixture of features typical of either vanadium dioxide or sesquioxide, which we developed in the previous sections.

We are nevertheless left with the question why the compound V_7O_{13} does not undergo an MIT. From purely structural considerations the main difference between V_7O_{13} and V_8O_{15} is the amount of dioxide-like center sites. The local environments and thus the electronic properties of the individual sites are very similar. However, we point out that the MITs in the Magnéli series arise as combinations of an embedded Peierls instability inherent in the metal chains and electronic correlations relevant for the chain end atoms. Since compounds with small vanadium chains are dominated by chain end sites and thus more susceptible to correlations, their MITs are most likely driven by sesquioxide-like states. On the other hand, the Peierls mechanism should be dominating for materials with long chains. This scenario of different driving forces of the MITs is consistent with the behaviour of the transition temperatures in the Magnéli series as seen in figure 1. With only one exception ($n = 5$) the temperatures decrease monotonously from V_3O_5 to V_7O_{13} , which does not show a transition. In the case of V_5O_9 the peculiar superstructure evolving below the MIT might cause the observed deviation. Transferred to our picture this kind of systematics corresponds to the decreasing influence of chain end sites as compared to the growing impact of the chain centers. When the chain length increases the influence of the local electronic correlations at the chain ends diminishes. At the same time the Peierls-like mechanism becomes stronger. With an increasing number of chain center atoms available for V-V dimerization the energy gain resulting from such a modification becomes more and more advantageous. With the experimental transition temperatures in mind we thus attribute the MIT of V_8O_{15} to a Peierls-like scheme; for V_7O_{13} neither of the two mechanisms is strong enough to induce a transition.

8 Conclusions

The vanadium Magnéli phases V_nO_{2n-1} form a homologous series of compounds with crystal structures comprising dioxide and sesquioxide-like regions. Studying the MITs in this material class thus paves the way for a more complete understanding of the phase transitions of the prototypical oxides VO_2 ($n \rightarrow \infty$) and V_2O_3 ($n = 2$). Analyzing those V $3d$ t_{2g} states which are involved in the phase transitions allows us to discuss the changing influence of electronic correlations and electron-lattice interaction on going from VO_2 to V_2O_3 . We have developed a unifying description of the various crystal structures including both the rutile structure of VO_2 and the corundum structure of V_2O_3 . Our systematic representation is based on a regular three-dimensional network of oxygen octahedra partially filled by metal atoms, giving rise to characteristic metal chains of length n . Due to the comprehensive picture of the structures, the electronic bands can be grouped into states behaving either VO_2 or V_2O_3 -like. The detailed electronic structure and consequently the MITs of the Magnéli phases turn out to be strongly influenced by the local metal-metal coordination. The phase transitions arise as results of both electron lattice interaction within the dioxide-like and electronic correlations within the sesquioxide-like regions of the crystal. Dioxide-like vanadium sites reveal the characteristic features of the embedded Peierls instability responsible for the MIT of VO_2 . The combination of dimerization and antiferroelectric-like displacements of the metal atoms by means of strong electron-lattice interaction causes splitting of the $d_{x^2-y^2} = d_{||}$ states and energetical upshift of the d_{yz}/d_{xz} states. Sites related to V_2O_3 are characterized by strongly reduced V-V overlap. Thus the $d_{x^2-y^2}$ states become more localized. Consequently, correlation effects play a more important role for these states. In conclusion, the electronic structures and the metal-insulator transitions of the Magnéli phases remain a crucial test case for theories aiming at a correct description of both VO_2 and V_2O_3 .

Acknowledgements We are grateful to U. Eckern for many fruitful discussions as well as for his continuous support. Discussions with S. Horn, S. Klimm, T. Kopp, P. Pfalzer, and K. Schwarz are acknowledged. This work was supported by the Deutsche Forschungsgemeinschaft (Sonderforschungsbereich 484, Augsburg).

References

- [1] J. B. Goodenough, *Prog. Solid State Chem.* **5**, 145 (1971).
- [2] W. Brückner, H. Oppermann, W. Reichelt et al., *Vanadiumoxide* (Akademie-Verlag, Berlin, 1983).
- [3] M. Imada, A. Fujimori, and Y. Tokura, *Rev. Mod. Phys.* **70**, 1039 (1998).
- [4] A. Magnéli, *Acta Chem. Scand.* **2**, 501 (1948).
- [5] S. Andersson and L. Jahnberg, *Ark. Kemi* **21**, 413 (1963).
- [6] S. Kachi, K. Kosuge, and H. Okinaka, *J. Solid State Chem.* **6**, 258 (1973).
- [7] G. D. Khattak, P. H. Keesom, and S. P. Faile, *Phys. Rev. B* **18**, 6181 (1978).
- [8] S. Nagata, P. H. Keesom, and S. P. Faile, *Phys. Rev. B* **20**, 2886 (1979).
- [9] A. C. Gossard, J. P. Remeika, T. M. Rice, and H. Yasuoka, *Phys. Rev. B* **9**, 1230 (1974).
- [10] M. Marezio, D. B. McWhan, P. D. Dernier, and J. P. Remeika, *Phys. Rev. Lett.* **28**, 1390 (1972).
- [11] B. F. Griffing, S. A. Shivashankar, S. Nagata et al., *Phys. Rev. B* **25**, 1703 (1982).
- [12] B. F. Griffing, S. A. Shivashankar, S. P. Faile, and J. M. Honig, *Phys. Rev. B* **31**, 8143 (1985).
- [13] A. C. Gossard, F. J. Di Salvo, L. C. Erich et al., *Phys. Rev. B* **10**, 4178 (1974).
- [14] P. C. Canfield, J. D. Thompson, and G. Gruner, *Phys. Rev. B* **41**, 4850 (1990).
- [15] D. B. McWhan, M. Marezio, J. P. Remeika, and P. D. Dernier, *Phys. Rev. B* **10**, 490 (1974).
- [16] P. I. Sorantin and K. Schwarz, *Inorg. Chem.* **31**, 567 (1992).
- [17] F. J. Morin, *Phys. Rev. Lett.* **3**, 34 (1959).
- [18] M. Marezio, D. B. McWhan, J. P. Remeika, and P. D. Dernier, *Phys. Rev. B* **5**, 2541 (1972).
- [19] J. P. Pouget, H. Launois, J. P. D'Haenens et al., *Phys. Rev. Lett.* **35**, 873 (1975).
- [20] J. P. Pouget and H. Launois, *J. Phys. (France)* **C4-37**, 49 (1976).
- [21] J. M. Longo and P. Kierkegaard, *Acta Chem. Scand.* **24**, 420 (1970).
- [22] V. Eyert, R. Horny, K.-H. Höck, and S. Horn, *J. Phys.: Cond. Matt.* **12**, 4923 (2000).
- [23] V. Eyert, *Europhys. Lett.* **58**, 851 (2002).
- [24] V. Eyert, *Ann. Phys. (Leipzig)* **11**, 650 (2002).
- [25] R. E. Peierls, *Quantum Theory of Solids* (Clarendon, Oxford, 1955).
- [26] G. Grüner, *Rev. Mod. Phys.* **60**, 1129 (1988).
- [27] N. F. Mott, *Rev. Mod. Phys.* **40**, 677 (1968).
- [28] F. Gebhard, *The Mott Metal-Insulator Transition* (Springer, Berlin, 1997).
- [29] D. Maurer, A. Leue, R. Heichele, and V. Müller, *Phys. Rev. B* **60**, 13249 (1999).
- [30] H. W. Verleur, A. S. Barker Jr., and C. N. Berglund, *Phys. Rev.* **172**, 788 (1968).
- [31] E. Goering, M. Schramme, O. Müller et al., *Phys. Rev. B* **55**, 4225 (1997).
- [32] O. Müller, E. Goering, J.-P. Urbach et al., *J. Phys. IV (France)* **C2-7**, 533 (1997).
- [33] S. Shin, S. Suga, M. Taniguchi et al., *Phys. Rev. B* **41**, 4993 (1990).
- [34] A. Zylbersztejn and N. F. Mott, *Phys. Rev. B* **11**, 4383 (1975).
- [35] V. Eyert, *Habilitation thesis, Universität Augsburg* (1998).
- [36] R. M. Wentzcovitch, W. W. Schulz, and P. B. Allen, *Phys. Rev. Lett.* **72**, 3389 (1994); *ibid.* **73**, 3043 (1994); T. M. Rice, H. Launois, and J. P. Pouget, *ibid.* **73**, 3042 (1994).
- [37] D. B. McWhan, J. P. Remeika, T. M. Rice et al., *Phys. Rev. Lett.* **27**, 941 (1971).
- [38] D. B. McWhan, A. Menth, J. P. Remeika et al., *Phys. Rev. B* **7**, 1920 (1973).
- [39] H. Kuwamoto, J. M. Honig, and J. Appel, *Phys. Rev. B* **22**, 2626 (1980).
- [40] P. D. Dernier and M. Marezio, *Phys. Rev. B* **2**, 3771 (1970).
- [41] P. D. Dernier, *J. Phys. Chem. Solids* **31**, 2569 (1970).
- [42] P. Pfalzer, J. Will, A. Nateprov Jr. et al., *Phys. Rev. B* **66**, 085119 (2002).
- [43] C. Castellani, C. R. Natoli, and J. Ranninger, *Phys. Rev. B* **78**, 4945 (1978).
- [44] L. F. Mattheiss, *J. Phys.: Cond. Matt.* **6**, 6477 (1994).
- [45] M. J. Rozenberg, G. Kotliar, H. Kajueter et al., *Phys. Rev. Lett.* **75**, 105 (1995).
- [46] S. Shin, Y. Tezuka, T. Kinoshita et al., *J. Phys. Soc. Jpn.* **64**, 1230 (1995).
- [47] K. E. Smith and V. E. Henrich, *Phys. Rev. B* **50**, 1382 (1994).
- [48] O. Müller, J. P. Urbach, E. Goering et al., *Phys. Rev. B* **23**, 15056 (1997).
- [49] J.-H. Park, L.-H. Tjeng, A. Tanaka et al., *Phys. Rev. B* **61**, 11506 (2000).
- [50] S. Yu. Ezhov, V. I. Anisimov, D. I. Khomskii, and G. A. Sawatzky, *Phys. Rev. Lett.* **83**, 4136 (1999).
- [51] F. Mila, R. Shiina, F.-C. Zhang et al., *Phys. Rev. Lett.* **85**, 1714 (2000).
- [52] I. S. Elfimov, T. Saha-Dasgupta, and M. A. Korotin, *Phys. Rev. B* **68**, 113105 (2003).
- [53] W. Bao, C. Broholm, G. Aeppli et al., *Phys. Rev. Lett.* **78**, 507 (1997).
- [54] K. Held, G. Keller, V. Eyert et al., *Phys. Rev. Lett.* **86**, 5345 (2001).
- [55] S.-K. Mo, J. D. Denlinger, H.-D. Kim et al., *Phys. Rev. Lett.* **90**, 186403 (2003).

- [56] M. S. Laad, L. Craco, and E. Müller-Hartmann, Phys. Rev. Lett. **91**, 156402 (2003).
- [57] H. Horiuchi, M. Tokonami, N. Morimoto, and K. Nagasawa, Acta Cryst. **B28**, 1404 (1972).
- [58] M. Marezio, D. B. McWhan, P. D. Dernier, J. P. Remeika, J. Solid State Chem. **6**, 419 (1973).
- [59] J.-L. Hodeau and M. Marezio, J. Solid State Chem. **23**, 253 (1978).
- [60] P. C. Canfield, Ph.D. thesis, University of California, Los Angeles (1990).
- [61] Y. Le Page und P. Strobel, J. Solid State Chem. **43**, 314 (1982).
- [62] H. Horiuchi, N. Morimoto, and M. Tokonami, J. Solid State Chem. **17**, 407 (1976).
- [63] T. Hahn (Ed.), International Tables for Crystallography (Kluwer Academic, Dordrecht, 1989).
- [64] S. Åsbrink, Acta Cryst. **B36**, 1332 (1980).
- [65] S. Hong und S. Åsbrink, Acta Cryst. **B38**, 713 (1982).
- [66] A. R. Williams, J. Kübler, and C. D. Gelatt Jr., Phys. Rev. B **19**, 6094 (1979).
- [67] V. Eyert, Int. J. Quantum Chem. **77**, 1007 (2000).
- [68] S. H. Vosko, L. Wilk, and M. Nusair, Can. J. Phys. **58**, 1200 (1980).
- [69] V. Eyert and K.-H. Höck, Phys. Rev. B **57**, 12727 (1998).
- [70] V. Eyert, Ph.D. thesis, Technische Hochschule Darmstadt (1991).
- [71] U. Schwingenschlögl, Ph.D. thesis, Universität Augsburg (2004), <http://www.physik.uni-augsburg.de/theo2/>.
- [72] U. Schwingenschlögl, V. Eyert, and U. Eckern, Europhys. Lett. **61**, 361 (2003).
- [73] U. Schwingenschlögl, V. Eyert, and U. Eckern, Europhys. Lett. **64**, 682 (2003).
- [74] Y. Le Page, P. Bordet, and M. Marezio, J. Solid State Chem. **92**, 380 (1991).
- [75] M. Marezio, P. D. Dernier, D. B. McWhan, and S. Kachi, J. Solid State Chem. **11**, 301 (1974).